Geosci. Model Dev., 11, 283–304, 2018
https://doi.org/10.5194/gmd-11-283-2018

Geoscientific Model Development
Open Access
EGU

The CarbonTracker Data Assimilation System for CO_2 and $\delta^{13}C$ (CTDAS-C13 v1.0): retrieving information on land–atmosphere exchange processes

Ivar R. van der Velde[1,2,3], John B. Miller[2], Michiel K. van der Molen[1], Pieter P. Tans[2], Bruce H. Vaughn[4], James W. C. White[4], Kevin Schaefer[5], and Wouter Peters[1,6]

[1]Department of Meteorology and Air Quality, Wageningen University and Research, Wageningen, the Netherlands
[2]Global Monitoring Division, NOAA Earth System Research Laboratory, Boulder, CO, USA
[3]Cooperative Institute for Research in Environmental Sciences, University of Colorado, Boulder, CO, USA
[4]Institute for Arctic and Alpine Research, University of Colorado, Boulder, CO, USA
[5]National Snow and Ice Data Center, University of Colorado, Boulder, CO, USA
[6]Centre for Isotope Research, University of Groningen, Groningen, the Netherlands

Correspondence: Ivar van der Velde (ivar.vandervelde@noaa.gov)

Received: 25 March 2017 – Discussion started: 30 May 2017
Revised: 26 September 2017 – Accepted: 13 November 2017 – Published: 22 January 2018

Abstract. To improve our understanding of the global carbon balance and its representation in terrestrial biosphere models, we present here a first dual-species application of the CarbonTracker Data Assimilation System (CTDAS). The system's modular design allows for assimilating multiple atmospheric trace gases simultaneously to infer exchange fluxes at the Earth surface. In the prototype discussed here, we interpret signals recorded in observed carbon dioxide (CO_2) along with observed ratios of its stable isotopologues $^{13}CO_2/^{12}CO_2$ ($\delta^{13}C$). The latter is in particular a valuable tracer to untangle CO_2 exchange from land and oceans. Potentially, it can also be used as a proxy for continent-wide drought stress in plants, largely because the ratio of $^{13}CO_2$ and $^{12}CO_2$ molecules removed from the atmosphere by plants is dependent on moisture conditions.

The dual-species CTDAS system varies the net exchange fluxes of both $^{13}CO_2$ and CO_2 in ocean and terrestrial biosphere models to create an ensemble of $^{13}CO_2$ and CO_2 fluxes that propagates through an atmospheric transport model. Based on differences between observed and simulated $^{13}CO_2$ and CO_2 mole fractions (and thus $\delta^{13}C$) our Bayesian minimization approach solves for weekly adjustments to both net fluxes and isotopic terrestrial discrimination that minimizes the difference between observed and estimated mole fractions.

With this system, we are able to estimate changes in terrestrial $\delta^{13}C$ exchange on seasonal and continental scales in the Northern Hemisphere where the observational network is most dense. Our results indicate a decrease in stomatal conductance on a continent-wide scale during a severe drought. These changes could only be detected after applying combined atmospheric CO_2 and $\delta^{13}C$ constraints as done in this work. The additional constraints on surface CO_2 exchange from $\delta^{13}C$ observations neither affected the estimated carbon fluxes nor compromised our ability to match observed CO_2 variations. The prototype presented here can be of great benefit not only to study the global carbon balance but also to potentially function as a data-driven diagnostic to assess multiple leaf-level exchange parameterizations in carbon-climate models that influence the CO_2, water, isotope, and energy balance.

1 Introduction

The terrestrial biosphere has absorbed about 25 % of global fossil fuel carbon dioxide (CO_2) emissions over the last several decades but the future of this sink is highly uncertain in a warming world (Booth et al., 2012; Rowlands et al., 2012). It depends on the small difference between two large fluxes

of the terrestrial carbon cycle: photosynthetic uptake or gross primary production (GPP) and terrestrial ecosystem respiration (TER), and is here referred to as the net ecosystem exchange (NEE = TER − GPP + fire disturbances and land use change and harvesting of crops). All these flux terms respond to changes in local temperature, precipitation, nutrient availability, and other key environmental variables (Friedlingstein et al., 2006). Extreme climate events such as droughts can decrease GPP and increase TER and fire disturbances to a point where regional NEE is turned into a temporary carbon source (Ciais et al., 2005; Gatti et al., 2014; van der Laan-Luijkx et al., 2015). These dynamic responses (and positive feedbacks whereby increased CO_2 may lead to more droughts) are now an integral part of climate models that include fully coupled carbon cycling (Booth et al., 2012; Dai , 2012). Such models give rise to a wide range of climate projections primarily as a result of different simulations of terrestrial carbon exchange (Friedlingstein et al., 2006). It is therefore important to test and improve the representation of the terrestrial biosphere in carbon-climate models. Uncertainty in climate projections can be reduced by evaluating present-day performance of these models to observations (Hoffman et al., 2014). This paper presents a data assimilation system that can be used to evaluate existing terrestrial biosphere models by using an extensive number of atmospheric CO_2 observations in tandem with other trace gases.

Measurements of atmospheric CO_2 have been used to infer carbon fluxes at the Earth's surface using a variety of inversion techniques (e.g., Keeling and Revelle, 1985; Keeling et al., 1989; Tans et al., 1993; Ciais et al., 1995; Rayner et al., 2008; Alden et al., 2010). Unfortunately, a limited number of CO_2 observations, errors in atmospheric transport modeling, and the realism of bottom-up carbon flux estimates are limiting the utility of these techniques. For instance, the representation of subgrid scale vertical motion in (and through the top of) the planetary boundary layer is one of the most uncertain aspects in atmospheric tracer modeling and can hinder the accuracy of CO_2 transport (Kretschmer et al., 2012; Miller et al., 2015). In addition, atmospheric CO_2 as a tracer has its own limitations as it only reflects a small residual of different sources and sinks, such as wild fires, anthropogenic sources, ocean in- and outgassing, and terrestrial GPP and TER.

The CarbonTracker Data Assimilation System (CTDAS) has been developed to estimate global net ocean and terrestrial carbon exchange fluxes, with a focus on North America and Europe (Peters et al., 2005, 2007, 2010; van der Laan-Luijkx et al., 2017). This application uses the ensemble Kalman filter (EnKF) as a Bayesian minimization approach for the estimation of weekly ocean and terrestrial carbon fluxes on a $1^\circ \times 1^\circ$ horizontal grid to improve the agreement between modeled and measured atmospheric CO_2. The versatile object-oriented design of CTDAS allows flexible implementation of different components of the data assimilation system (van der Laan-Luijkx et al., 2017). Such modifications include but are not limited to (1) the configuration of the state vector; (2) the expansion of the monitoring network, such as for the Amazon (van der Laan-Luijkx et al., 2015) and China (Zhang et al., 2014); (3) the use of Lagrangian atmospheric transport (He et al., in preparation); and (4) to monitor other tracer gases like methane (Bruhwiler et al., 2014; Tsuruta et al., 2016).

One aspect that has not yet been explored in CTDAS is the monitoring of multiple trace gases in the atmosphere that are strongly related (i.e., gases with a common chemical or metabolic pathway in the ocean and/or terrestrial biosphere). The main purpose of such an application is to improve the estimation of carbon fluxes and to retrieve new information on the underlying flux exchange processes that would otherwise remain undetected. We are in particular interested in the use of the stable isotope ^{13}C (in atmospheric CO_2) as an additional tracer alongside total CO_2 to estimate carbon sources and sinks and their variability. In earlier studies, ^{13}C was used to distinguish oceanic from terrestrial carbon exchange, as oceans take up $^{13}CO_2$ more efficiently than land surfaces relative to $^{12}CO_2$. In so-called double-deconvolution methods this particular trait is used to untangle the global land carbon budget from the ocean carbon budget (Keeling et al., 1989; Tans et al., 1993; Ciais et al., 1995). More recently, the ^{13}C isotope was used to study the diurnal cycle of GPP and TER (Wehr et al., 2016) and was used as a tracer of water use efficiency to study long-term responses to CO_2 increases in tree rings (van der Sleen et al., 2015), and attempts are underway to do the same based on atmospheric records. On regional scales, variations in the ratio of $^{13}CO_2/^{12}CO_2$ (typically reported as $\delta^{13}C$ in ‰ relative to the VPDB reference ratio) reflect changes in discrimination processes associated with photosynthetic uptake of carbon by plants (e.g., Farquhar et al., 1989; Fung et al., 1997; Scholze et al., 2003; Rayner et al., 2008). Plants generally take up the heavier $^{13}CO_2$ molecules less efficiently than $^{12}CO_2$ molecules, increasing the $^{13}CO_2/^{12}CO_2$ ratio of CO_2 remaining in the atmosphere. This kind of discrimination against ^{13}C is much stronger for C_3 plants than for C_4 plants, but also varies as a function of moisture conditions in the canopy air and soil (Farquhar et al., 1980, 1989; Ekblad and Högberg, 2001; Ometto et al., 2002; Suits et al., 2005). That implies that under the right circumstances, measured atmospheric $\delta^{13}C$ can be used to recognize land usage, such as C_3/C_4 photosynthesis, and changes in photosynthetic activity resulting from drought stress (Ballantyne et al., 2010; Raczka et al., 2016).

Such an application could also be beneficial to explore other facets of carbon exchange. Any errors in the fossil fuel emission inventories (although relatively small) are in the current CTDAS releases aliased erroneously on the natural ocean and terrestrial fluxes. Assimilation of the fraction of the radioactive isotope $^{14}CO_2$ in the atmosphere would allow independent verification of the fossil fuel emissions as its old organic carbon is radiocarbon-free (Bozhinova et al., 2014; Basu et al., 2016). Other chemical constituents like carbonyl sulfide (OCS) and solar-induced chlorophyll fluo-

rescence (SIF) could also be important additions to CTDAS. Inclusion of these tracers in the assimilation could enhance our understanding of carbon exchange, because variations in photosynthetic carbon uptake are recorded in atmospheric OCS and satellite SIF data (Yang et al., 2014; Commane et al., 2015).

Before we can interpret signals derived from these additional tracers, our aim for this paper is (1) to explain how the first dual-species CTDAS application works, with a specific focus on the use of $\delta^{13}C$ and CO_2, henceforth the system named as CTDAS-C13 version 1.0; (2) to demonstrate its accuracy in solving the targeted optimization problem in comparison to observations; (3) to test the sensitivity of the system to the introduced nonlinearity arising from simultaneous optimization of terrestrial total CO_2 and $^{13}CO_2$ fluxes; and (4) to verify our new estimates of carbon and isotope exchange with independent drought index data.

2 Methodology

We present the atmospheric $\delta^{13}C$ budget (Sect. 2.1) before proceeding to describe the integration of $\delta^{13}C$ within our new dual-species data assimilation framework CTDAS-C13 (Sect. 2.2). We then briefly describe the prior estimates and the observational network used (Sect. 2.3). Finally, we give a brief description of the different inversion experiments (Sect. 2.4). The methodology presented here is based on Sect. 4.2 of the lead author's PhD dissertation (van der Velde, 2015).

2.1 Atmospheric $\delta^{13}C$ budget

The use of $\delta^{13}C$ observations alongside CO_2 observations constitute a useful change to the traditional CO_2-only CTDAS application, as it provide an additional constraint on carbon surface fluxes and isotope exchange processes in plants. The rationale behind this is that the $^{13}CO_2$ and $^{12}CO_2$ contents in the atmosphere are affected through the same CO_2 pathways from land and ocean surfaces. There are, however, specific processes that change the $^{13}CO_2$ exchange fluxes slightly differently from $^{12}CO_2$ fluxes. We can write a global mass balance for atmospheric $\delta^{13}C$ (δ_a) so that the different isotopic processes are explicitly defined and dependent on total CO_2 fluxes (for the derivation of Eq. 1 see Tans et al., 1993). We can then identify the (1) emission forcing terms, (2) net exchange isotope forcing terms, and (3) gross-flux isodisequilibrium forcing terms:

$$\begin{aligned} C_a \frac{d}{dt}\delta_a = {} & F_{ff}(\delta_{ff} - \delta_a) + F_{fire}(\delta_{fire} - \delta_a) \\ & \text{[emission forcing terms]} \\ & + N_b \epsilon_{ph} + N_o \epsilon_{ao} \\ & \text{[net exchange isotope terms]} \\ & + F_{ba}\left(\delta_b - \delta_b^{eq}\right) \\ & \text{[terrestrial isodisequilibrium forcing terms]} \\ & + F_{oa}\left(\delta_a^{eq} - \delta_a\right) \\ & \text{[ocean isodisequilibrium forcing term]}, \end{aligned} \quad (1)$$

where C_a is the total carbon content (unit mol or mass) in the atmosphere (in the form of CO_2). The subscripts ba and oa denote the direction of the one-way gross fluxes (unit mol or mass per unit time). For example, F_{ba} refers to the respiratory release of CO_2 from terrestrial biosphere to atmosphere. The isotopic ratios of $^{13}C/^{12}C$ are expressed as δ_{xx} (‰), where the subscripts refer to the signature in biosphere vegetation and soils (b), in biomass burning flux (fire), or in the fossil fuel emission flux (ff). The signature δ_a^{eq} depicts the isotopic ratio of CO_2 that is in equilibrium with the ocean surface and δ_b^{eq} depicts the ratio in the terrestrial biosphere that would be in isotopic equilibrium with the current atmosphere, which is more depleted in $^{13}CO_2$ than when the biomass was formed years ago. N_b and N_o refer to net exchange fluxes (gross release minus gross uptake) of CO_2, and F_{ff} and F_{fire} are the fossil fuel and biomass burning CO_2 emissions, respectively.

The terrestrial (photosynthetic) isotopic discrimination in Eq. (1) is expressed as $\epsilon_{ph} = \left(\delta_b^{eq} - \delta_a\right) \approx -\Delta_{ph}$ (‰), and can be derived from a CO_2 gradient-weighted average of different isotope fractionation effects during the transfer of CO_2 molecules from the canopy air until their reaction with the enzyme Ribulose-1,5-bisphosphate (Rubisco) in the chloroplasts of the plant leaf. There are two main fractioning effects along this pathway: the plant fractionates with $\Delta_s = 4.4$ ‰ when CO_2 diffuses from leaf boundary through leaf stomata, and with $\Delta_f = 28$ ‰ during carboxylation. Smaller fractionation effects occur during diffusion between canopy air and leaf boundary ($\Delta_b = 2.9$ ‰), and during dissolution of CO_2 in mesophyll water ($\Delta_{diss} = 1.1$ ‰) and transport to chloroplasts ($\Delta_{aq} = 0.7$ ‰). The parameterization of Δ_{ph} for C_3 plants has been described by Farquhar et al. (1982) and takes the following form as in Suits et al. (2005):

$$\begin{aligned} \Delta_{ph} = {} & \Delta_b\left(\frac{c_a - c_s}{c_a}\right) + \Delta_s\left(\frac{c_s - c_i}{c_a}\right) \\ & + \left(\Delta_{diss} + \Delta_{aq}\right)\left(\frac{c_i - c_c}{c_a}\right) + \Delta_f\left(\frac{c_c}{c_a}\right), \end{aligned} \quad (2)$$

where $c_{a,\,s,\,i,\,c}$ represent CO_2 partial pressures in canopy air space, leaf boundary layer, stomatal cavity, and in the chloroplasts, respectively. The overall discrimination Δ_{ph} value reflects mostly the fractionation step with the highest resistivity (O'Leary, 1988). For example, during a drought when the leaf's stomatal conductance is lowered in an attempt to prevent evaporative water loss, the diffusive Δ_s is the most limiting factor resulting in a lower overall Δ_{ph}. The opposite happens under more favorable environmental conditions when stomatal aperture is higher and carboxylation is the limiting factor, resulting in a higher overall Δ_{ph}.

The overall discrimination leaves the atmosphere relatively enriched and plants relatively depleted in ^{13}C. C_3

plants are depleted in ^{13}C by approximately $-20‰$ relative to the atmosphere and C_4 by approximately $-4‰$ as they can assimilate $^{13}CO_2$ more efficiently with Rubisco. C_4 photosynthesis is essentially a more complex form of carbon fixation than C_3 photosynthesis as it shields Rubisco in the bundle sheath cells from wastefully binding with oxygen rather than carbon dioxide.

In addition to discrimination effects during photosynthetic uptake, we also need to account for isotopic enrichment of the atmosphere through respiratory release of carbon with a heavier isotopic signature after spending from one year to several decades or more in the plant and soil organic matter. This respiratory part will still enrich the atmosphere with $^{13}CO_2$ even if net CO_2 uptake equals zero (Ciais et al., 1995), and we refer to it as the terrestrial isodisequilibrium flux in Eq. (1).

Discrimination associated with the dissolution of CO_2 in ocean water (Zhang et al., 1995) is much smaller and spatiotemporally homogeneous ($\epsilon_{ao} = -2‰$) than in the terrestrial biosphere. The difference between ocean and land discrimination provide an additional constraint on the net fluxes and has already been demonstrated in previous studies (e.g., Keeling et al., 1989; Tans et al., 1993; Ciais et al., 1995; Fung et al., 1997; Rayner et al., 2008). We also have to account for isotopic disequilibrium that exists between the atmosphere and oceans. This isodisequilibrium flux is associated with the outgassing of CO_2 from the ocean waters, and has globally an enriching tendency on the δ_a signatures.

Besides the land and ocean discrimination and disequilibrium forcing terms we have two additional terms in Eq. (1). Firstly, there are CO_2 emissions due to combustion of fossil fuels, which have a distinct isotopic signature depending on the organic fuel type, but globally its signature is approximately $\delta_{ff} = -30‰$. Secondly, there are CO_2 emissions due to biomass burning, where δ_{fire} bears the signature of the $^{13}CO_2$ and $^{12}CO_2$ fluxes of F_{fire}, which is typically the signature of burnt leaf foliage, woody tissue, and the aboveground litter (van der Velde et al., 2014).

2.2 CTDAS-C13

We followed the method presented by Peters et al. (2005) for designing the joint CO_2 and δ_a data assimilation system. The architecture is similar to the CarbonTracker Data Assimilation Shell (CTDAS) v1.0 discussed in detail by van der Laan-Luijkx et al. (2017). Just like the traditional CO_2-only inversions, we aim to close the CO_2 budget through fluxes from fossil fuel combustion, biomass burning, and net exchange fluxes from the terrestrial biosphere and oceans. In addition, we also intend to simultaneously close the $^{13}CO_2$ ($^{13}C_a$) budget using the same set of CO_2 fluxes. Isotopic signatures themselves are not conserved quantities, therefore we calculate conserved mole fractions of CO_2 and $^{13}CO_2$ in our transport model, which we can sample at designated locations and times to calculate δ_a. The combined set of balance equations (unit mol per unit time) takes the following form:

$$\frac{\mathrm{d}}{\mathrm{d}t}C_a = F_{ff} + F_{fire} + \lambda_b N_b + \lambda_o N_o, \quad (3)$$

$$\frac{\mathrm{d}}{\mathrm{d}t}{}^{13}C_a = {}^{13}F_{ff} + {}^{13}F_{fire} + {}^{13}N_b + {}^{13}N_o. \quad (4)$$

After some manipulation of Eqs. (3) and (4), by following Tans et al. (1993), we obtain the following:

$$\frac{\mathrm{d}}{\mathrm{d}t}{}^{13}C_a = F_{ff}R_{ff} + F_{fire}R_{fire} + \lambda_b N_b \left(\lambda_{discr}\epsilon_{ph}/1000 + 1\right) R_a + \lambda_o N_o \left(\epsilon_{ao}/1000 + 1\right) R_a + D_b + D_o. \quad (5)$$

The $^{13}C_a$ balance equation is now a close analog of Eq. (1), because $^{13}C_a$ is a function of discrimination, N_b and N_o, and isodisequilibrium fluxes. The R values depict the isotopic ratio of $^{13}CO_2/CO_2$ in the atmosphere (R_a), in fossil fuel (R_{ff}), and biomass burning emissions (R_{fire}), and their values are approximately 0.011. The isodisequilibrium fluxes from land and ocean surfaces are here simply shown as D_b and D_o, respectively. The term $\left(\lambda_{discr}\epsilon_{ph}/1000 + 1\right)$ represents the optimized ratio between the isotopic signature in the photosynthetic flux and atmosphere (R_{ph}/R_a), and ranges between 0.980 and 0.996 depending on the prior ϵ_{ph} and discrimination scaler λ_{discr}. The term $(\epsilon_{ao}/1000 + 1)$ represents the ocean flux ratio and is held constant at 0.998 assuming $\epsilon_{ao} = -2‰$, and is not optimized. The parameters λ_b and λ_o represent the linear scaling factors for each week and ecosystem region (ecoregion) to adjust the net carbon exchange over land and ocean surfaces, respectively. For land, the scaling factor is associated with one scalar per ecoregion based on the Olson (1985) land use classification following Peters et al. (2005, 2007) (Fig. 1). The terrestrial biosphere is further divided into 11 larger geographical areas also known as TransCom regions (Gurney et al., 2002). Like in the early CarbonTracker releases, each of the 11 TransCom land regions contains a maximum of 19 ecoregion types (Fig. 2) and the ocean is divided into 30 large basins encompassing large-scale ocean circulation features. This gives a maximum of 239 ($= 11 \cdot 19 + 30$) different scaling factors each week (Peters et al., 2007). The new parameter is λ_{discr}, which is used to scale a maximum of 209 terrestrial discrimination parameters per week. They are associated with the same $1° \times 1°$ ecoregions as the terrestrial fluxes. Note that the maximum number of scalable land parameters is in reality ~ 130, and not 209, because not each land region contains all 19 ecoregion types.

The terrestrial net exchange term in Eq. (5) $\left(\lambda_b N_b \left(\lambda_{discr}\epsilon_{ph}/1000 + 1\right) R_a\right)$ includes two multiplicative scaling factors, making the required solution nonlinear. This poses a potential problem where variations in net exchange and discrimination are canceling each other out to such a degree that it leads to low signal-to-noise ratios, especially for discrimination. This is further investigated

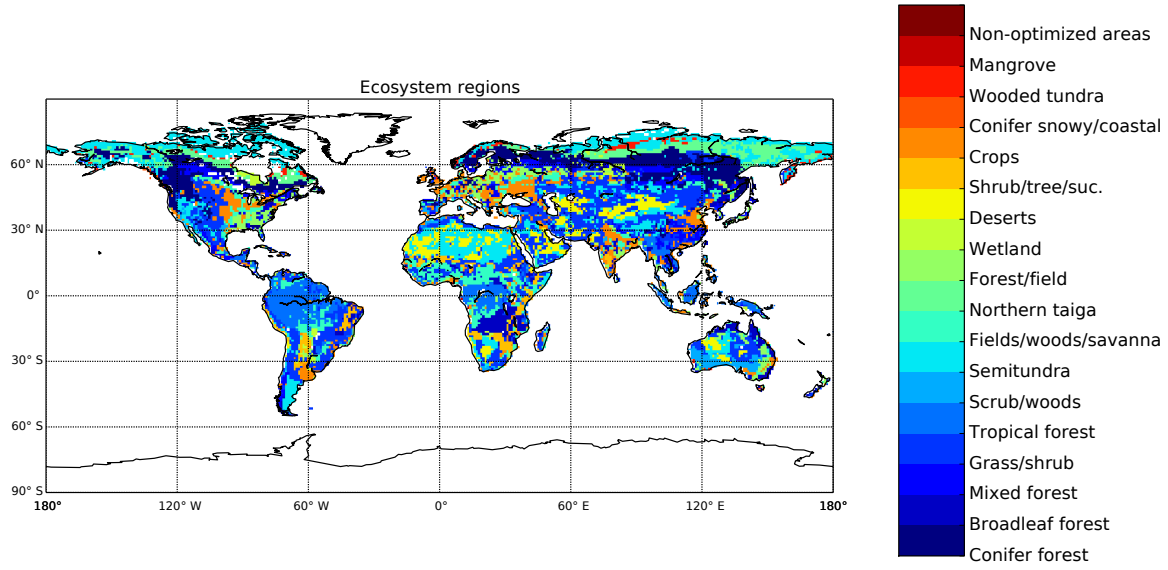

Figure 1. Global distribution of Olson ecosystem types.

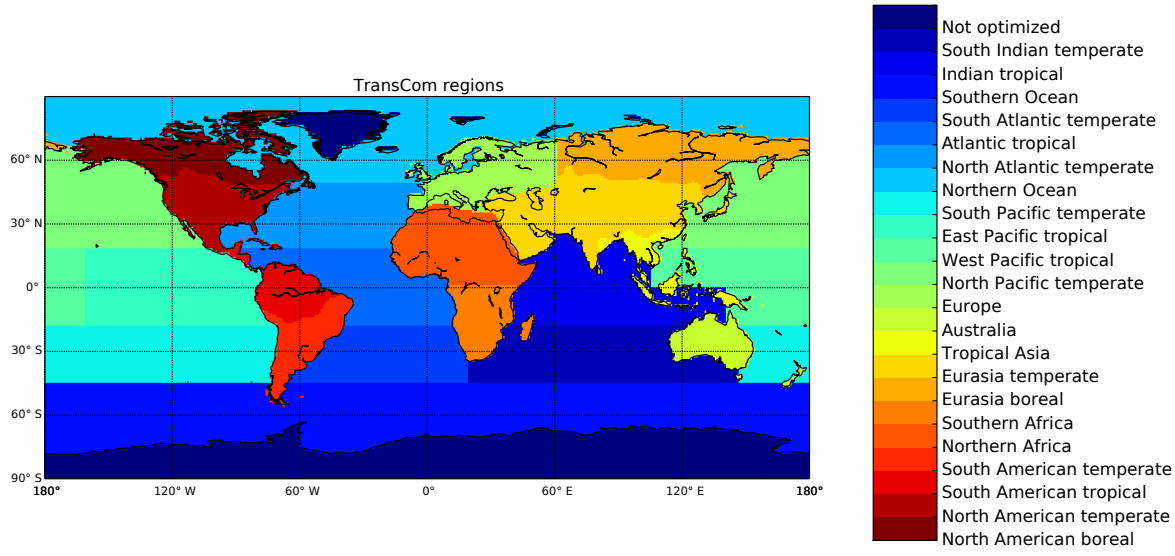

Figure 2. Earth's partitioning into 11 land regions and 11 ocean regions according to the TransCom project. The ocean regions are divided into 30 smaller basins (not shown) and the land regions can contain up to 19 different ecoregions as shown in Fig. 1.

in Sect. 3.2. The fossil fuel combustion, biomass burning, and terrestrial and ocean isodisequilibrium fluxes all remain fixed a priori estimates. We describe in Sect. 3.1 the tuning of the latter disequilibrium fluxes to close the long-term mean balance of $\delta^{13}C$ in our system.

The scaling factors λ_b, λ_o, and λ_{discr} are the unknowns that are combined in state vector $\boldsymbol{x}$ (with dimension s), for which we will try to find an optimal solution by minimizing a quadratic cost function. In this function, there is a balance between information drawn from the observation vector $\boldsymbol{y}$ (with dimension m) with a covariance $\mathbf{R}$ (m × m) and prior knowledge from the state vector $\boldsymbol{x}_p$ (s) with a covariance $\mathbf{P}$ (s × s):

$$J = (\boldsymbol{y} - H(\boldsymbol{x}))^T \mathbf{R}^{-1} (\boldsymbol{y} - H(\boldsymbol{x})) + (\boldsymbol{x} - \boldsymbol{x}_p)^T \mathbf{P}^{-1} (\boldsymbol{x} - \boldsymbol{x}_p). \quad (6)$$

The observation operator H (m) represents the atmospheric transport model that propagates the surface fluxes from Eqs. (3) and (5) and samples accordingly the mole fractions of CO_2 and $^{13}CO_2$ at the same location and moment as the observations $\boldsymbol{y}$.

The solution for $\boldsymbol{x}$ that minimizes J is (Tarantola, 2005)

$$\boldsymbol{x} = \boldsymbol{x}_\mathrm{p} + \mathbf{K} \cdot \left[\boldsymbol{y} - H\left(\boldsymbol{x}_\mathrm{p}\right) \right], \tag{7}$$

where $\mathbf{K}$ represents the Kalman gain matrix (Peters et al., 2005). Equation (7) can be expressed in terms of λ (posterior scaling factor), λ_p (prior scaling factor), and separate measurements of CO_2 (c) and $\delta^{13}C$ (δ) with dimensions (j) and (k), respectively:

$$\begin{pmatrix} \lambda_{\mathrm{bio1}} \\ \cdot \\ \cdot \\ \lambda_{\mathrm{bio209}} \\ \lambda_{\mathrm{oce210}} \\ \cdot \\ \cdot \\ \lambda_{\mathrm{oce239}} \\ \lambda_{\mathrm{discr240}} \\ \cdot \\ \cdot \\ \lambda_{\mathrm{discr448}} \end{pmatrix} = \begin{pmatrix} \lambda_{p_{\mathrm{bio1}}} \\ \cdot \\ \cdot \\ \lambda_{p_{\mathrm{bio209}}} \\ \lambda_{p_{\mathrm{oce210}}} \\ \cdot \\ \cdot \\ \lambda_{p_{\mathrm{oce239}}} \\ \lambda_{p_{\mathrm{discr240}}} \\ \cdot \\ \cdot \\ \lambda_{p_{\mathrm{discr448}}} \end{pmatrix} + \mathbf{K} \cdot \left[\begin{pmatrix} \mathrm{c}_1 \\ \mathrm{c}_2 \\ \mathrm{c}_3 \\ \mathrm{c}_4 \\ \cdot \\ \cdot \\ \mathrm{c}_\mathrm{j} \\ \delta_1 \\ \delta_2 \\ \delta_3 \\ \delta_4 \\ \cdot \\ \cdot \\ \delta_k \end{pmatrix} - H \begin{pmatrix} \lambda_{p_{\mathrm{bio1}}} \\ \cdot \\ \cdot \\ \lambda_{p_{\mathrm{bio209}}} \\ \lambda_{p_{\mathrm{oce210}}} \\ \cdot \\ \cdot \\ \lambda_{p_{\mathrm{oce239}}} \\ \lambda_{p_{\mathrm{discr240}}} \\ \cdot \\ \cdot \\ \lambda_{p_{\mathrm{discr448}}} \end{pmatrix} \right]. \tag{8}$$

In state vectors $\boldsymbol{x}$ and $\boldsymbol{x}_\mathrm{p}$, the scaling factors for terrestrial discrimination are appended after the flux scaling factors. Similarly in the observation vectors $\boldsymbol{y}$ and $H(\boldsymbol{x}_\mathrm{p})$, the $\delta^{13}C$ observations are appended after the CO_2 observations. The $\mathbf{K}$ matrix determines how much a scaling factor needs to change given a set of CO_2 and $\delta^{13}C$ measurements. The matrices $\mathbf{R}$ and $\mathbf{P}$ modulate whether observations or bottom-up estimates are given more weight to the solution.

The $\mathbf{P}$ matrix contains 448×448 elements in total and is shown in Fig. 3. The first 209×209 element block contains the land flux uncertainties per ecoregion and their spatial correlations. The second 30×30 element block contains the ocean flux uncertainties per ocean basin. We gave the land scalars and the ocean scalars a maximum uncertainty of 80 and 100 % along the diagonal, respectively, as in earlier CarbonTracker releases. The third 209×209 element block contains the terrestrial discrimination scalars with a maximum uncertainty of 20 % along the diagonal with an identical spatial correlation structure as applied to the terrestrial flux uncertainty scalars. This implies that we can scale ϵ_{ph} by a factor of 1.0 ± 0.2, and thus for a typical C_3 plant ($\epsilon_{\mathrm{ph}} = -20$ ‰) the mean and uncertainty lies around -20 ± 4 ‰. Furthermore, there is covariation between ecoregions of nearby TransCom regions, e.g., between North America boreal and temperate regions and between Europe and Eurasian regions. We did not allow covariances between net exchange and discrimination in order to give the parameters enough freedom in the solution.

The covariance structure of $\mathbf{R}$ is similar to CO_2-only CTDAS, but is extended with additional uncertainties in $\delta^{13}C$ observations. These expected uncertainties quantify our ability to simulate observations given the uncertainty in atmospheric transport modeling and measurement errors. Section 2.3.5 gives an overview of the used uncertainties for each observation category.

With this inversion framework in place CTDAS-C13 progresses in a similar manner as the traditional CO_2-only CTDAS. For each week, the set of unknowns in the state vector are updated in a cycle that contains two steps. First there is a forecast step, which is driven by our fluxes and current background state vector $\boldsymbol{x}_\mathrm{p}$ to forecast an ensemble of CO_2 and $^{13}CO_2$ mole fractions 5 weeks ahead in time. This is followed by an analysis step to determine the new state of the system with Eq. (8) such that it is consistent with the observations for the current week of the cycle. The analyzed state is propagated to the next cycle using the same model as Peters et al. (2007, Eq. 1 of the Supplement), and with this new state a new cycle begins with another forecast step to forecast a new ensemble of the background state 5 weeks ahead in time, now with an additional set of observations from a new week. The ensemble for each tracer is created from 150 ensemble members to provide a Gaussian probability density function of the state vector.

The simulation of atmospheric transport is provided by the two-way nested global transport model TM5 release 3 (Krol et al., 2005). This application simulates the atmospheric transport of CO_2 and $^{13}CO_2$ at a global $6° \times 4°$ resolution, with no nesting. It is driven by 3 hourly meteorological output from ECMWF ERA-Interim reanalysis (Dee et al., 2011). All the CO_2 and $^{13}CO_2$ flux fields provided to the model are in units of mol CO_2 m^{-2} s^{-1} and mol $^{13}CO_2$ m^{-2} s^{-1}, respectively. Atmospheric concentrations of CO_2 and $^{13}CO_2$ are calculated as mole fractions in mol mol^{-1}. Signatures of $\delta^{13}C$ are computed to the relative per mil value using the following conversion formulation in order to facilitate comparison with observations:

$$\delta^{13}\mathrm{C} = \left(\frac{R}{R_{\mathrm{ref}}} - 1 \right) \cdot 1000, \tag{9}$$

where R_{ref} is the VPDB reference ratio adopted for $^{13}CO_2/(^{12}CO_2 + {}^{13}CO_2)$, which is 0.011112 (Tans et al., 1993). R is the ratio of simulated mole fractions $^{13}CO_2/CO_2$.

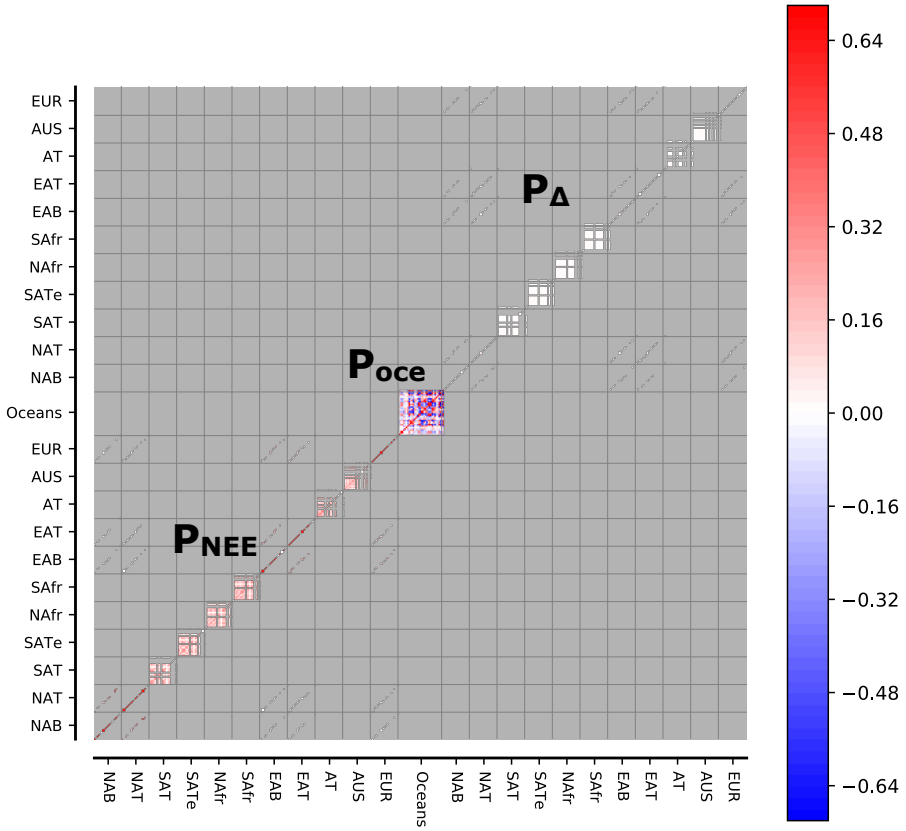

Figure 3. The prior **P** covariance structure represents squared uncertainty of the dimensionless state vector. The first 209×209 element block represents the covariance matrix for land NEE with a maximum diagonal uncertainty of 0.64 (equivalent to 80 %), the second 30×30 element block represents the covariance matrix for ocean fluxes with a maximum diagonal uncertainty of 1.0 (equivalent to 100 %), and the third 209×209 element block represents the covariance matrix for Δ_{ph} with a maximum diagonal uncertainty of 0.04 (equivalent to 20 %). The matrix is organized according to TransCom ocean basins and land regions, where each land region contains 19 potential ecoregions (see Figs. 1 and 2).

2.3 Prior estimates and observations

2.3.1 Terrestrial biosphere fluxes

The terrestrial first-guess net CO_2 exchange (N_b) and fire (F_{fire}) estimates were calculated in the Simple-Biosphere Carnegie–Ames–Stanford Approach model (SiB-CASA; Schaefer et al., 2008) on a $1° \times 1°$ grid on a 10 min time resolution and were further processed into 3 hourly mean fluxes to serve as input for CTDAS-C13. SiBCASA is a biogeochemical model that calculates carbon, isotope, water, and energy exchange fluxes. The model inherited the aerodynamic and surface resistance models from SiB (Sellers et al., 1996) to solve for CO_2 partial pressures in an iterative loop to acquire a balance between net assimilation rate, stomatal conductance, mesophyll conductance, and CO_2 partial pressures. The aerodynamic resistance model describes the turbulent transfer processes using the Monin–Obuhkov similarity theory. The surface and interior resistance models describe the pathway of CO_2 (but also water and heat) through the leaf boundary, the leaf stomata, and ultimately the leaf chloroplasts. The Ball–Berry–Collatz model is used to estimate stomatal conductance (Ball, 1988; Collatz et al., 1991) and is coupled to the Farquhar and Collatz photosynthesis models for C_3 and C_4 vegetation (Farquhar et al., 1980; Collatz et al., 1992). A mesophyll conductance formulation was introduced by Suits et al. (2005) to predict realistic CO_2 partial pressures in the chloroplasts. Mesophyll conductance is suggested to be as important as stomatal conductance in terms of magnitude and variability, and it is shown that $\delta^{13}C$ correlate more precisely with c_c/c_a than with c_i/c_a (Flexas et al., 2008). It is parameterized as a function of the canopy photosynthetic rate and soil water stress factor. SiBCASA is driven by 3 hourly ECMWF ERA-Interim meteorology, designed with a semi-prognostic leaf pool to track seasonal plant phenology, and it uses GFED4 daily burned area disturbances to calculate fire fluxes at a fine temporal resolution (van der Velde et al., 2013, 2014). The model incorporates 12 different aggregated ecosystems according to Olson (1985) to calculate photosynthesis. Respiratory CO_2 release

from the plant and soil is calculated in the CASA part of the model using 13 biogeochemical pools with environment-influenced turnover rates (Schaefer et al., 2008).

2.3.2 Ocean fluxes

The ocean first-guess net CO_2 exchange (N_o) estimates derive from ocean inversions from Jacobson et al. (2007). These long-term estimates are combined with the quadratic gas-transfer velocity from 3 hourly ECMWF ERA-Interim wind fields (Wanninkhof, 1992) to create fluxes on a $1^\circ \times 1^\circ$ grid at a 3 hourly temporal resolution. An additional trend was applied to the fluxes to ensure that increases in anthropogenic uptake are proportional to increases in atmospheric CO_2 levels (see http://www.esrl.noaa.gov/gmd/ccgg/carbontracker).

2.3.3 Fossil fuel emissions

Fossil fuel CO_2 emissions (F_{ff}) were made available on $1^\circ \times 1^\circ$ grid at a monthly temporal resolution. They are derived from a combination of databases: EDGAR4.2, CDIAC, and BP statistics (see http://www.esrl.noaa.gov/gmd/ccgg/carbontracker).

2.3.4 Isotope and disequilibrium fluxes

To calculate the fluxes of $^{13}CO_2$ from land surfaces we used the photosynthetic discrimination parameterization (Eq. 2) for C_3 plants in the SiBCASA model (van der Velde et al., 2014). The weighted leaf-level value for C_3 discrimination is typically 19.0 ‰, and given the more efficient CO_2 bonding with the Rubisco enzyme, C_4 discrimination is 4.4 ‰ (Still et al., 2003; Suits et al., 2005). Given the dominance of C_3 plant growth (70 % of global GPP), the global mean discrimination in SiBCASA has been estimated at $\Delta_{ph} = 15.2$ ‰. SiBCASA's spatial heterogeneity of land discrimination is shown in Fig. 4. It reflects the land use distribution and the environmental forcing. Large discrimination values can be found in the temperate regions, the boreal forests, and in the humid environments such as the tropical rain forests in South America, Africa, and South East Asia. Small discrimination values can be found in the United States corn belt and in the dry climate regions such as the African savannas and Australian grasslands, where there is an abundance of C_4 plant growth. More subtle variations in Δ_{ph} in C_3 dominant regions are driven by differences in environmental conditions (e.g., humidity, groundwater availability, and light intensity). Weekly $1^\circ \times 1^\circ$ fields for Δ_{ph} were used to map the regular 3 hourly net CO_2 fluxes to $^{13}CO_2$ fluxes:

$$[\text{terrestrial net } ^{13}\text{C exchange term}] = \lambda_b N_b \left(\lambda_{discr}\epsilon_{ph}/1000 + 1\right) R_a, \quad (10)$$

where ϵ_{ph} is derived from SiBCASA's Δ_{ph} output. Their relation is straightforward

$$\epsilon_{ph} = -\Delta_{ph}. \quad (11)$$

For the calculation of $^{13}CO_2$ biomass burning flux we assumed R_{fire} to be very close to the signature of newly assimilated photosynthates:

$$^{13}F_{fire} = F_{fire}\left(\lambda_{discr}\epsilon_{ph}/1000 + 1\right) R_a. \quad (12)$$

The $^{13}CO_2$ fossil fuel emissions are calculated with $R_{ff} = 0.0107786$, given that the global mean value of δ_{ff} is equal to -30 ‰:

$$^{13}F_{ff} = F_{ff} R_{ff}. \quad (13)$$

Note that we did not vary δ_{ff} for different fuel types in this version of CTDAS-C13, but such variability could be included in the future based on the work of Andres et al. (2000).

The ocean discrimination parameter ϵ_{ao} is assumed to be constant at -2 ‰ as in many comparable studies (e.g., Tans et al., 1993; Ciais et al., 1995; Alden et al., 2010), and is not optimized. The regular 3 hourly net CO_2 fluxes were mapped to $^{13}CO_2$ fluxes as follows:

$$[\text{ocean net } ^{13}\text{C exchange term}] = \lambda_o N_o \left(\epsilon_{ao}/1000 + 1\right) R_a, \quad (14)$$

The isodisequilibrium fluxes (D_b and D_o, in mol $^{13}CO_2\,m^{-2}\,s^{-1}$) were made available on a monthly $1^\circ \times 1^\circ$ resolution. D_b is calculated using SiBCASA's gross natural respiratory flux scaled with isotopic disequilibrium of the terrestrial biosphere with the current atmosphere, i.e., $F_{ba}\left(\delta_b - \delta_b^{eq}\right)$. Because fossil fuel emissions add isotopically depleted CO_2 to the atmosphere, the biosphere signature δ_b follows with a time lag dependent on the residence time of carbon in the vegetation and soils. That implies δ_b is larger than δ_b^{eq}, which is the biosphere signature that is in equilibrium with the current atmosphere (Tans et al., 1993). D_b has a positive tendency on atmospheric $\delta^{13}C$ as carbon originating from different SiBCASA pools is older and more enriched in ^{13}C than the isotopic signature of recently fixed photosynthates. The SiBCASA pool configuration is described in detail in van der Velde et al. (2014).

D_o is calculated from the outgassing flux of CO_2 scaled with the isotopic disequilibrium of the ocean surface with the current atmosphere, i.e., $F_{oa}\left(\delta_a^{eq} - \delta_a\right)$. The δ_a^{eq} term is determined from a global network of $\delta^{13}C$ measurements in dissolved inorganic carbon (Gruber et al., 1999). F_{oa} is parameterized as a function of surface ocean partial pressure of CO_2 and wind speed after Takahashi et al. (2009). Wind speed and solubility are assumed to remain constant year-to-year. The disequilibrium fluxes are positive from the equator to approximately 60° of latitude in both directions and are negative beyond that.

2.3.5 Observations

Observations of CO_2 from a wide range of research laboratories are bundled in Observation Package (ObsPack) version 1.0.3 and observations of $\delta^{13}C$ from the INSTAAR Stable Isotope Lab are bundled in version 1.0.0. These are data

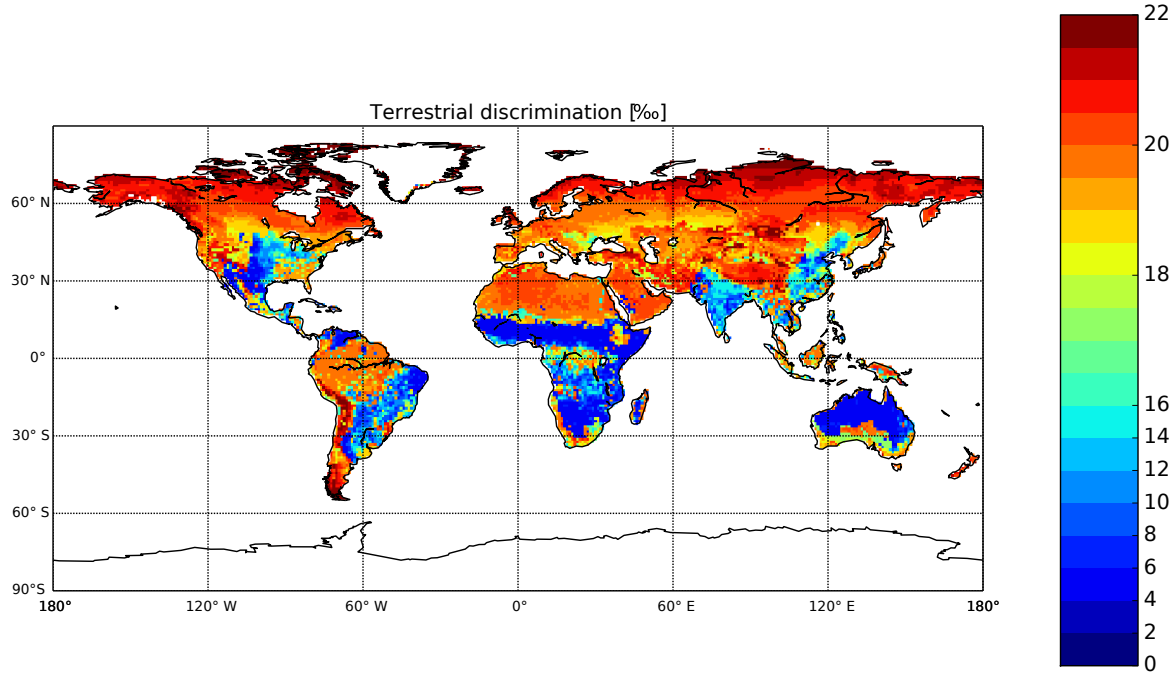

Figure 4. Mean (2001–2011) modeled discrimination parameter Δ_{ph} (‰) from SiBCASA. The discrimination is more detailed for $\Delta_{ph} > 16$‰ to highlight the more subtle variations in Δ_{ph} in the dominant C_3 regions that experience different environmental forcing.

products that include the provider's original data and metadata reformatted into the ObsPack framework (Masarie et al., 2014).

From the available CO_2 observations, approximately 24 000 weekly flask measurements were used in the assimilation from a fixed network of 58 surface sites. Another large set of 174 000 measurements came from 23 semi-continuous in situ sites. Most CO_2 measurements are obtained with a nominal precision of ±0.1 ppm. The remainder of sites and measurements (including from aircraft or shipboard) were not used because of double records, and some measurements were kept for independent checks. A small fraction was omitted as our model could not resolve certain locations at a coarse resolution.

For the dual-species inversions we also used 22 000 flask measurements of $\delta^{13}C$ from 53 different surface sites. A further 5600 measurements from five different sites were obtained using programmable flask packages, which measure $\delta^{13}C$ at a daily resolution. The isotope ratios are measured by dual inlet mass spectrometry with a precision of ±0.01 ‰.

We determined observation uncertainties (model–data mismatch or MDM) for each of the $\delta^{13}C$ measurement sites in a heuristic manner based on earlier test inversions. These values are added to the diagonal of **R**. A too small error would give an unrealistic amount of confidence how well the model is expected to represent the measurement location during sampling but a too large error would give very little confidence to the measurement representation.

Table 1. Summary of assigned $\delta^{13}C$ model–data mismatch (MDM), the category-averaged and 1σ SD of the innovation χ^2, and number of sites per category.

Site category	MDM (‰)	χ^2	No. of sites
land	0.13	0.97 ± 0.52	10
mixed	0.080	0.80 ± 0.34	11
marine boundary layer	0.03	1.29 ± 0.70	15
deep Southern Hemisphere	0.03	1.22 ± 0.44	07
problem	0.4	0.63 ± 0.48	10

The $\delta^{13}C$ measurement sites were divided into different categories each with their own MDM value. As with CO_2, these categories were land, mixed conditions, marine boundary layer, deep Southern Hemisphere, and a special category for problem sites where forecast performance is poor. For each site, we determined the innovation statistic χ^2, which is a measure for how apt our applied uncertainty level is given the model–data fit. A χ^2 value of 1.0 indicates that the simulated and expected total uncertainty are equal, lower values indicate overestimation of the uncertainty and higher values underestimation. Table 1 gives a summary of the site categories used, together with the assigned MDM for $\delta^{13}C$ and the category-average innovation χ^2 determined from an inversion experiment. For the majority of sites the innovation values are between 0.7 and 1.3, i.e., around the ideal value of

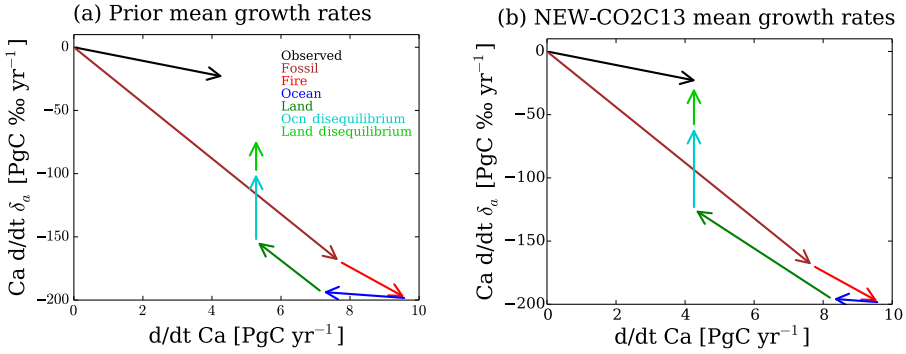

Figure 5. Annual mean carbon (x axis) and $\delta^{13}C$ (y axis) growth rates for **(a)** the prior estimates and for **(b)** the NEW−CO2C13 experiment. Colored arrows represent the different sources and sinks of the carbon cycle. A closed budget for both tracers was accomplished in the NEW−CO2C13 experiment, as indicated by the resultant vector (sum of all colored arrows) returning to the black arrow (observed growth rate in atmosphere). To close the long-term trend we increased the isodisequilibrium fluxes by 20 %.

Table 2. Summary of the four inversion experiments, the observations used, the optimized items (ocean and land fluxes, and Δ_{ph}), and their linearity. The prefix TRAD− refers to traditional, i.e., experiments that have been performed in the past in any way, shape or form. The prefix NEW− refers to a new type of inversions used in this publication. NEW−CO2C13 used the default CTDAS-C13 model setup as described in the Methodology, while NEW−2STEP solved for Δ_{ph} using only $\delta^{13}C$ data.

Experiment	Observations	Optimization	Linear?
TRAD−CO2	CO_2	flux only	yes
TRAD−CO2C13	CO_2 and $\delta^{13}C$	flux only	yes
NEW−CO2C13	CO_2 and $\delta^{13}C$	flux and Δ_{ph}	no
NEW−2STEP	$\delta^{13}C$	Δ_{ph} only	yes

1.0. For the CO_2 measurement sites we used a similar set of MDM values as in previous CarbonTracker releases.

2.4 Experiments

We performed four inversion experiments as summarized in Table 2. The simulation period covered the years 2000 through 2011, but our analyses focused on the period 2001–2011, i.e., we omitted the spin-up year. As a benchmark, we performed a traditional inversion to estimate the net carbon exchange fluxes of the ocean and land using only CO_2 observations, which we call TRAD−CO2. For the second inversion, we added $\delta^{13}C$ observations alongside CO_2 to constrain only the exchange fluxes; therefore, we call this experiment TRAD−CO2C13. The experiment in which we estimated discrimination and fluxes simultaneously is called NEW−CO2C13. This inversion is nonlinear because the discrimination scaling parameter is in the same multiplication term as the net flux scaling parameter. The fourth experiment was a linear inversion experiment where we estimated only the land discrimination parameter using $\delta^{13}C$ data. We call this experiment NEW−2STEP because discrimination was solved in a second step after optimization of the net exchange fluxes. This means that ocean and land fluxes were derived from the optimized state vector and its covariance from the TRAD−CO2 inversion.

3 Results

3.1 Comparison to observations of CO_2 and $\delta^{13}C$ from the global network

We first evaluate the global CO_2 and $\delta^{13}C$ budgets simulated by our combination of fluxes as described in Sect. 2 to assess where we expect the largest changes in the optimization. As shown in Fig. 5a, the prior net exchange flux estimates and unscaled disequilibrium fluxes were not large enough to close the gap with the observed tracers, CO_2, and $\delta^{13}C$. The sum of the flux arrows overestimated the annual CO_2 growth rate along the x axis and overestimated $\delta^{13}C$ depletion along the y axis. In a traditional TRAD−CO2 inversion, the estimated ocean and land fluxes closed the CO_2 budget along the x axis. The leverage in the net exchange fluxes was, however, not large enough to close the $\delta^{13}C$ budget along the y axis as well. In an inversion that includes $\delta^{13}C$ observations, the gap in $\delta^{13}C$ would adjust the CO_2 flux magnitudes and ocean/land partitioning to unrealistic magnitudes in an effort to overcome the large offset between the simulated and observed $\delta^{13}C$ growth rate. Instead we chose to use scaled disequilibrium fluxes in our inversions in order to estimate land and ocean CO_2 flux magnitudes that remain close to the results of other traditional carbon cycle budgeting studies (Alden et al., 2010; van der Velde et al., 2013). We chose the disequilibrium fluxes to adjust because (1) the exact magnitudes of these terms are still unknown due to uncertainties in the carbon pool turnover, gross carbon fluxes, and isotopic discrimination, and (2) these terms do not affect the CO_2 mass balance. It assured a closed mean $\delta^{13}C$ budget

of our inversions without creating unrealistic carbon sinks over land and oceans (Fig. 5b). Most importantly, closing the climatological (11 year) budget allowed us to focus our study on interannual changes in the net fluxes and photosynthetic discrimination.

We obtained the best fit with $\delta^{13}C$ data when the land and ocean disequilibrium flux were scaled by a factor of 1.2 without changing either their spatial patterns or time trends. This is consistent with recent double deconvolution studies where the global $\delta^{13}C$ balance was closed with a factor of 1.3 in land and ocean disequilibrium (Alden et al., 2010). Our value was determined after assessing an ensemble of different sets of scaling numbers (ranging from 1.1 to 1.5) in a forward TM5 simulation, which was driven by the optimized net land and ocean flux estimates from the TRAD−CO2 experiment. This assured a closed multi-year $\delta^{13}C$ budget together with a closed multi-year CO_2 budget. As selection criteria, we used (1) the 11 year mean root mean square difference (RMSD) of a large selection of $\delta^{13}C$ sites and (2) the average bias between simulated and observed values. In the non-scaled disequilibrium simulation we obtained a RMSD of 0.165 ‰ and a bias of −0.110 ‰ averaged over all sites. The optimal result was obtained with a scaling factor of 1.2, which reduced the RMSD to 0.079 ‰ and the mean bias to −0.010 ‰. Note that these scaling factors cannot be applied to other inversion studies because the disequilibrium scaling factors are tuned for this particular system and time period.

To demonstrate our procedure in terms of individual data sets, we refer to Fig. 6. After scaling the disequilibrium fluxes and using optimized net carbon exchange from the TRAD−CO2 inversion, time series of $\delta^{13}C$ at 32 of the 46 Northern Hemisphere sites showed no remaining significant trend (sites where p value > 0.05) in the summer residuals, and the residuals from the trend lines were within or close to the MDM specified for our dual-species inversions. Some of the sites with remaining trends are located at great distances from large continental carbon sources and sinks, and exert little influence on the posterior λ_{discr} parameter (e.g., CHR, GMI). Some of the other sites were assigned a large MDM (e.g., BAL, NWR, TAP) giving them less weight in the estimation of the posterior λ_{discr} parameter. The collection of sites with remaining trends do not seem to have a systematic geographic pattern and are likely reflecting a change in local oceanic or biospheric isotope exchange, such as must be the case for the Bermuda West (BMW, non-significant positive trend) and Bermuda East (BME, significant downward trend) site.

With the long-term trend of $\delta^{13}C$ appropriately captured, we proceeded to optimize NEE and Δ_{ph} with our new framework (NEW−CO2C13). We show that this inversion further reduced $\delta^{13}C$ residuals (Fig. 7a), without compromising (nor strongly improving) the fit to CO_2 (Fig. 7b) that we attained from the TRAD−CO2 inversion. In Fig. 7a the ratio of $\delta^{13}C$ RMSD of NEW−CO2C13 to $\delta^{13}C$ RMSD of the TRAD−CO2 inversions was at most sites smaller or equal to 0.95 (indicating a significantly higher accuracy of NEW−CO2C13 in form of bias and noise reduction):

$$\frac{\delta^{13}\text{C RMSD (NEW}-\text{CO2C13)}}{\delta^{13}\text{C RMSD (TRAD}-\text{CO2)}} < 0.95.$$

In Fig. 7b, the ratio of CO_2 RMSD of NEW−CO2C13 to CO_2 RMSD of TRAD−CO2 was at most locations between 0.95 and 1.05. This suggests that the two atmospheric constraints applied are complementary, and there is no indication that the TRAD−CO2 results from CarbonTracker were inconsistent with $\delta^{13}C$ measurements. This is an important prerequisite for a credible estimate of discrimination in our system. Furthermore, Fig. 7a shows a notable latitudinal divide in the reduction of $\delta^{13}C$ RMSD, indicating the utility of NEW−CO2C13 in the Northern Hemisphere due to the large availability of measurements and scalable discrimination parameters.

At sites like Alert (Nunavut, Canada) the NEW−CO2C13 inversion provided a better fit to the measured data than the TRAD−CO2 inversion (Fig. 8). The 11 year averaged $\delta^{13}C$ residuals were close to zero for both inversions, as the disequilibrium flux was tuned specifically to prevent large residuals in a-priori simulated $\delta^{13}C$ as described in Sect. 3.1. The 1σ SD of the $\delta^{13}C$ residuals at Alert were smaller in the NEW−CO2C13 inversion in comparison to TRAD−CO2 due to the additional optimization of Δ_{ph} alongside net exchange fluxes. The CO_2 residuals for Alert in Fig. 8 were for both inversions almost identical.

3.2 Linear and nonlinear estimates of net carbon uptake and land discrimination

Simultaneously optimizing both λ_{discr} and λ_{bio} is inherently nonlinear and thus possibly problematic for our assimilation system; therefore, we tested the validity of our approach in the NEW−CO2C13 inversion. We hypothesized that a region's net carbon uptake and discrimination would change in a similar fashion in the nonlinear inversion, as it would for a linear inversion. The linear inversion experiment consisted of two consecutive steps: (1) the optimization of the net exchange fluxes using only CO_2 observations (TRAD−CO2) followed by (2) the estimation of the land discrimination parameter using only $\delta^{13}C$ observations (NEW−2STEP). In the nonlinear NEW−CO2C13 inversion the optimization of fluxes and discrimination was done simultaneously. For net carbon uptake by vegetation, we refer to net ecosystem exchange or NEE defined as positive when CO_2 is taken up from the atmosphere. For plant isotope discrimination we refer to Δ_{ph} in per mil, which is defined as positive.

As shown in Fig. 9, the 11 year mean NEE for the 11 land TransCom regions are very similar in the nonlinear NEW−CO2C13 and linear TRAD−CO2 inversions. Deviations are in the order of tens of teragrams, and within 1σ SD of the flux interannual variability (IAV). Figure 9 also shows the impact of C_4 photosynthesis on the mean TransCom ag-

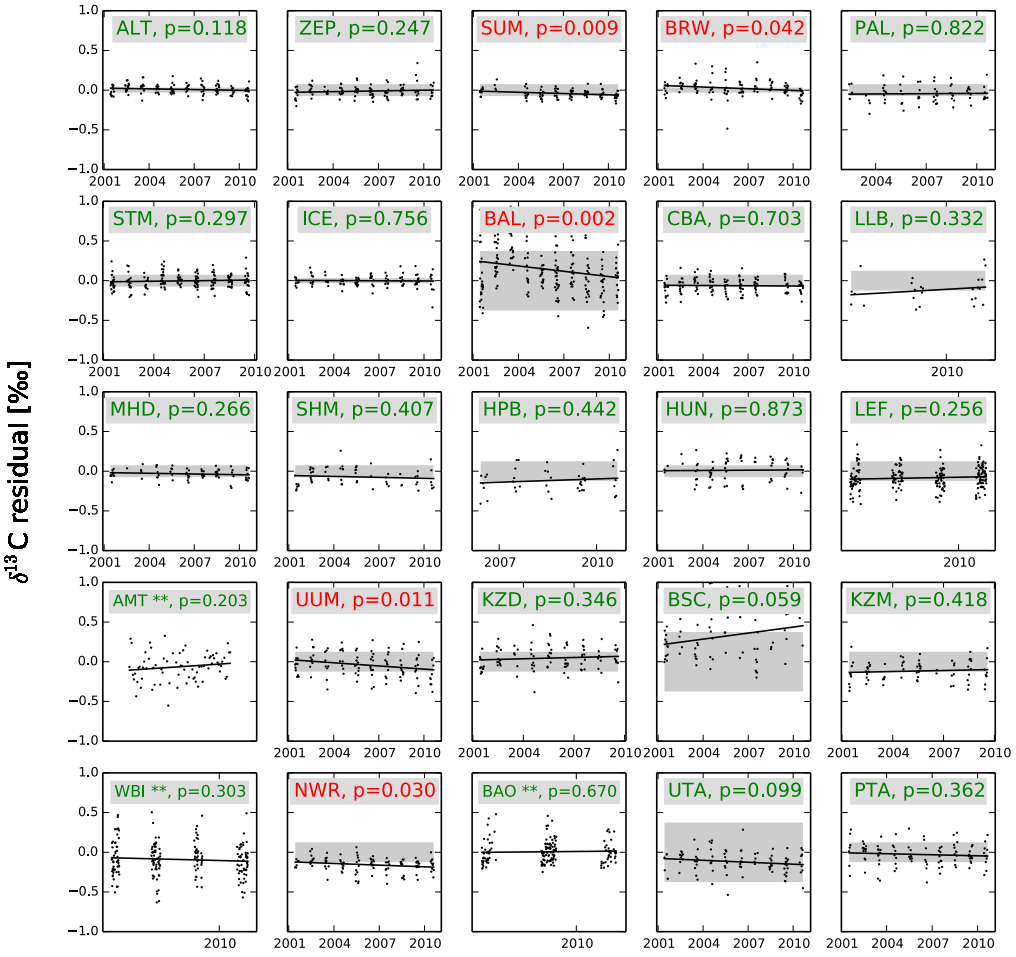

Figure 6.

gregated Δ_{ph} values. In the boreal regions, where there is very little C_4 plant growth, the discrimination is at its maximum (approximately 20 ‰, 5 ‰ above the global average), but in regions where there is C_4 plant growth (e.g., due to agriculture in the United States or savannas in Africa) the mean Δ_{ph} values are lower (approximately 12–15 ‰). These regional patterns of Δ_{ph} imposed by SiBCASA (see also Fig. 4) are maintained by the NEW−CO2C13 inversion framework. Because we aimed to retrieve robust temporal patterns of IAV, the most relevant indicators for the robustness of our nonlinear inversion approach are given by the correlation coefficients (r) between the two types of inversions. We calculated r for NEE and Δ_{ph} between the linear and nonlinear inversions. As the seasonal cycles in uptake and discrimination are largely dictated by the prior estimates, we removed them using a 3 month boxcar mean smooth curve fitting to obtain the anomalies relative to the seasonal trend. The NEE in NEW−CO2C13 is very similar to the NEE in TRAD−CO2, as indicated by the high r values (> 0.96 for $N = 52 \cdot 11$ weeks) for all TransCom regions. The r values are lower for Δ_{ph}, but still exceed 0.75 in the Northern Hemisphere. The correlation is particularly high over North America boreal, North America temperate, and European regions. Smaller correlations are obtained in tropical and temperate South America and tropical Asia. This is expected, however, as these regions typically suffer from a lack of observational constraints.

The linear NEW−2STEP inversion estimated the same large increase in discrimination IAV as in the nonlinear NEW−CO2C13 inversion for the Northern Hemisphere in comparison to the first-guess estimate of SiBCASA (8-fold increase in SD, see Table 3). In addition, we also found in both inversions a strong positive correlation between Δ_{ph} and NEE on annual time scales ($r = 0.79$) with a significant slope ($p = 0.001$, 95 % confidence interval of a two-sided distribution with 9 degrees of freedom). In years when annual mean NEE is low (less carbon uptake), the Δ_{ph} is low too (less discrimination), implying that stomata have partially closed, and vice versa. This correlation did not emerge in the TRAD−CO2 estimate based on atmospheric CO_2 observations alone, and it also did not emerge if $\delta^{13}C$ observations were additionally used in the TRAD−CO2C13 esti-

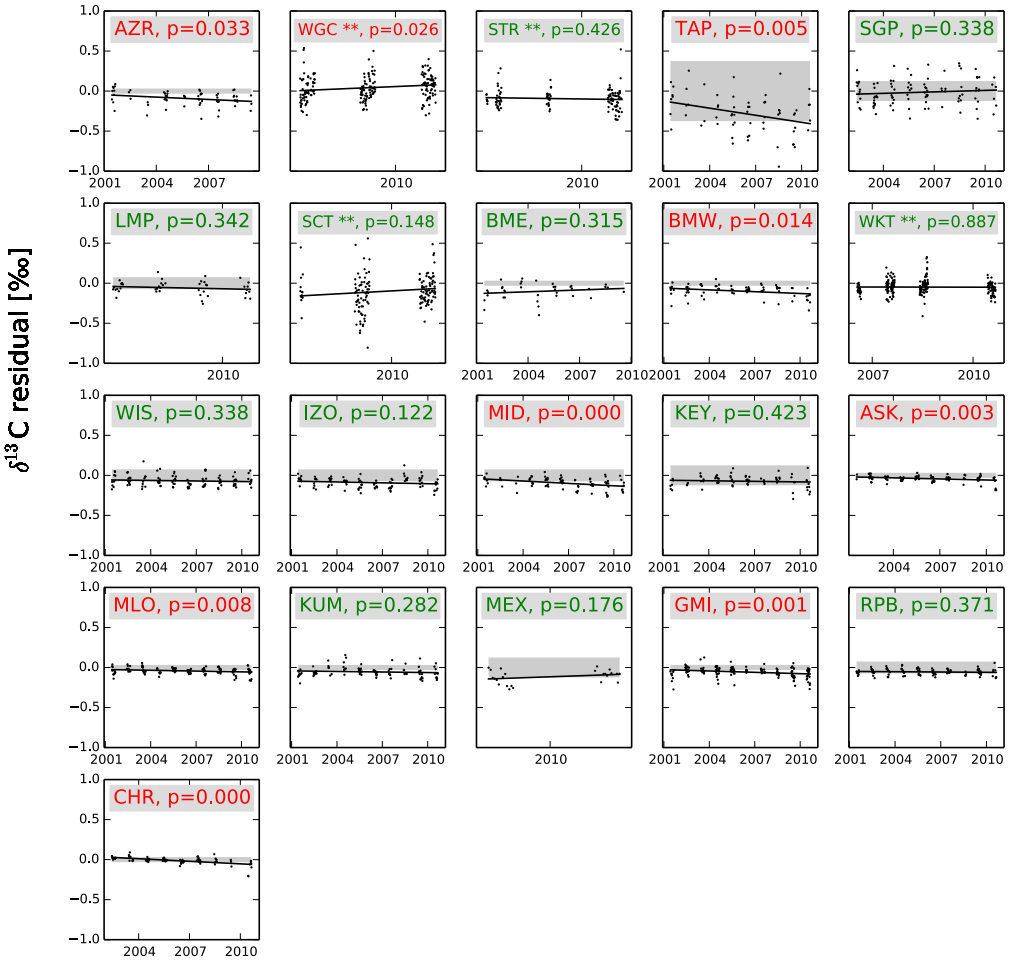

Figure 6. Summer (JJA) residuals of $\delta^{13}C$ (‰) in CO_2 for 46 sites (excluding aircraft and ships) situated in the Northern Hemisphere. These sites are ordered based on the their latitudinal location; most northern site is placed at the top left (Alert, Canada) and the site nearest to the equator at the bottom left in the second part of Fig. 6 (Christmas Island, Republic of Kiribati). All residuals (simulated minus observed) are calculated from a traditional TRAD−CO2 inversion with scaled disequilibrium fluxes. Assuming a closed long-term mean budget in $\delta^{13}C$, we tested the null hypothesis that the slope of the linear regression line is zero. Sites with a trend where the p value is smaller than the significance level of 5 % are shown in red, whereas the remaining sites without significant trend are shown in green. The sample uncertainty (model–data mismatch) used for the NEW−CO2C13 and NEW−2STEP inversions is displayed by transparent gray areas. Sites marked with ** were not included in the inversions but were used for independent verification. For detailed information of the sites and their locations, we refer to the NOAA website: http://www.esrl.noaa.gov/gmd/ccgg/carbontracker/observations.php.

Table 3. Northern Hemisphere land net carbon uptake (NEE, ($PgC\,yr^{-1}$)) and land discrimination (Δ_{ph}, (‰)) 11 year mean estimates, and IAV ($\pm 1\sigma$ SD) from SiBCASA (prior) and the four inversion experiments. The last row gives the correlation coefficient r between 11 annual mean NEE and Δ_{ph} values.

	Prior	TRAD−CO2	TRAD−CO2C13	NEW−CO2C13	NEW−2STEP
NEE	0.22 ± 0.28	2.44 ± 0.46	2.65 ± 0.49	2.58 ± 0.46	2.44 ± 0.46
Δ_{ph}	18.1 ± 0.02	18.1 ± 0.02	18.1 ± 0.02	18.2 ± 0.17	18.3 ± 0.17
r	−0.26	−0.14	−0.18	0.79	0.78

mate, to estimate NEE but not Δ_{ph}. The SiBCASA terrestrial biosphere model that provides the first-guess NEE and Δ_{ph} of our data assimilation framework based on commonly used drought response parameterizations, simulated neither the large IAV in NEE and Δ_{ph} nor their strong correlation. It is evident from the NEW−2STEP inversion that changes in

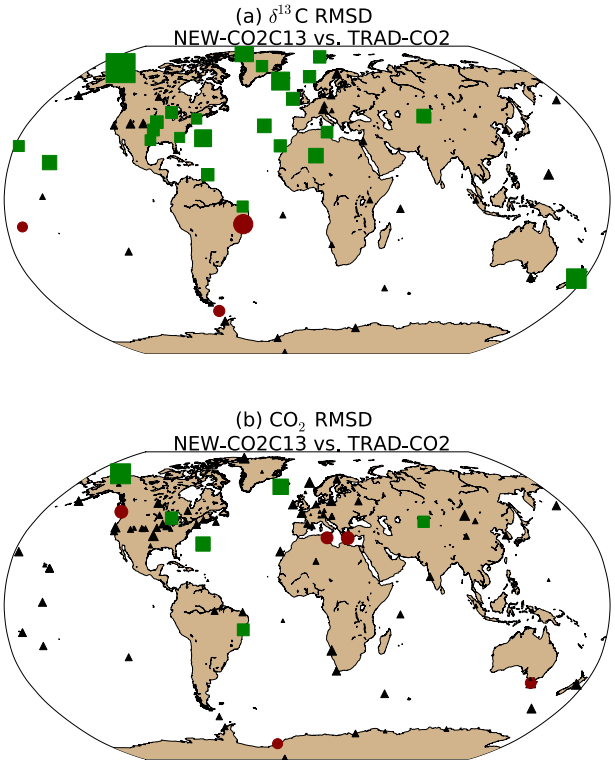

Figure 7. A comparison of the relative performance of inversion techniques for the period 2001 through 2006 based on the ratio of the model–data **(a)** $\delta^{13}C$ root mean square difference (RMSD) of NEW−CO2C13 to $\delta^{13}C$ RMSD of TRAD−CO2, and **(b)** CO_2 RMSD of NEW−CO2C13 to CO_2 RMSD of the TRAD−CO2 inversion. A ratio lower than 1.0 indicates a higher accuracy of the NEW−CO2C13 inversion technique; green sites indicate a ratio less than or equal to 0.95, red sites indicate a ratio greater than or equal to 1.05, and sites where the difference in respective RMSD is less than 0.05 are given in black. The size of each symbol is a measure of the relative performance of NEW−CO2C13 in comparison to TRAD−CO2. The larger the symbol the more the ratio of RMSD differs from 1.0.

Δ_{ph} and the correlation with NEE were driven by $\delta^{13}C$ observations, and were not a symptom of the systems inability to separately estimate NEE and Δ_{ph} variations. This suggests that the estimated IAV of Δ_{ph} in the nonlinear inversion is truly a signal retrieved from $\delta^{13}C$ that would otherwise be aliased erroneously into the carbon fluxes or not retrieved at all.

3.3 Independent verification with drought indices

A closer inspection reveals that the reported correlation between the Northern Hemisphere's NEE and Δ_{ph} in Table 3 could indicate a moisture-driven response on the ecosystem level. We identified several moments of severe to extreme drought as characterized by the Standardized Precipitation and Evaporation Index (SPEI; Vicente-Serrano et al., 2010) below −1.0 that covered an extensive area of more than a million square kilometers in the United States. These droughts are described in literature as the droughts (or heat waves) of summer 2002 (Seager, 2010; Schwalm et al., 2012) and 2011 (Long et al., 2013). The annual averaged maps of SPEI for 2001–2011 are shown in the top panel of Fig. 10 calculated for the Northern American temperate TransCom domain. Independent of the SPEI drought index, we estimated changes in Δ_{ph} and NEE over the same American domain with the NEW−CO2C13 inversion using atmospheric CO_2 and $\delta^{13}C$ data (Fig. 10 middle and lower panels). A correlation between Δ_{ph} and SPEI could only be established by applying an area weighting function to the SPEI index to give years that experienced large and severe droughts, the strongest association with reductions in Δ_{ph}. We used the following function for the Weighted Drought Index (WDI):

$$\text{WDI} = \frac{\sum_{i=1} (\text{SPEI}[i] \cdot \text{Grid-cell-area}[i])}{\text{Total-area}}.$$

In words, we sum over the product of the SPEI index and the grid cell surface area where SPEI is below −1.0 and subsequently we divide it by the total area of the TransCom domain. Hence, the WDI is an expression of the drought in terms of the surface area that is affected. A larger drought surface area will result in a more negative WDI. Using this function, we see that the lower values for Δ_{ph} correspond strongly with years of low SPEI over large serried areas, indicating a temporal correlation of $r = +0.75$ between the SPEI variable and Δ_{ph} (see correlation in Fig. 11 with a significant slope: $p = 0.008$, 95 % confidence interval of a two-sided distribution with 9 degrees of freedom). The two largest anomalies ($> 1\sigma$ of 11 year IAV) in annual mean Δ_{ph} correspond with low SPEI in 2002 and in 2011. A third notable drought as recorded in SPEI happened in 2006; although carbon uptake was reduced, it did not amount to a significant signal in Δ_{ph}. Similar correlations do exist over other parts of the Northern Hemisphere in our inversion solution. For instance, severe droughts in western Europe (2003) and Russia (2010) lowered the discrimination by 1.0 ‰, and exceeded more than 1σ SD of its 11 year IAV (not shown).

In addition, in years when Δ_{ph} is low, the annual mean NEE tends to be low too, possibly as a result of reduced GPP. This implies that leaf stomata have partially closed and are therefore affecting both Δ_{ph} and carbon uptake from photosynthesis. The reduction of the optimized net carbon sink for North America is 100–400 Tg C yr^{-1} during the drought years of 2002, 2006, and 2011 (in comparison to their surrounding years).

These correlations that are averaged over continent sized areas do, however, breakdown on smaller scales. On regional scales, we observed a partial misallocation of the model adjustments of NEE and Δ_{ph} in comparison to SPEI. This is largely a consequence of our limited capacity to monitor CO_2 and $\delta^{13}C$. For example, for North America temperate 2002,

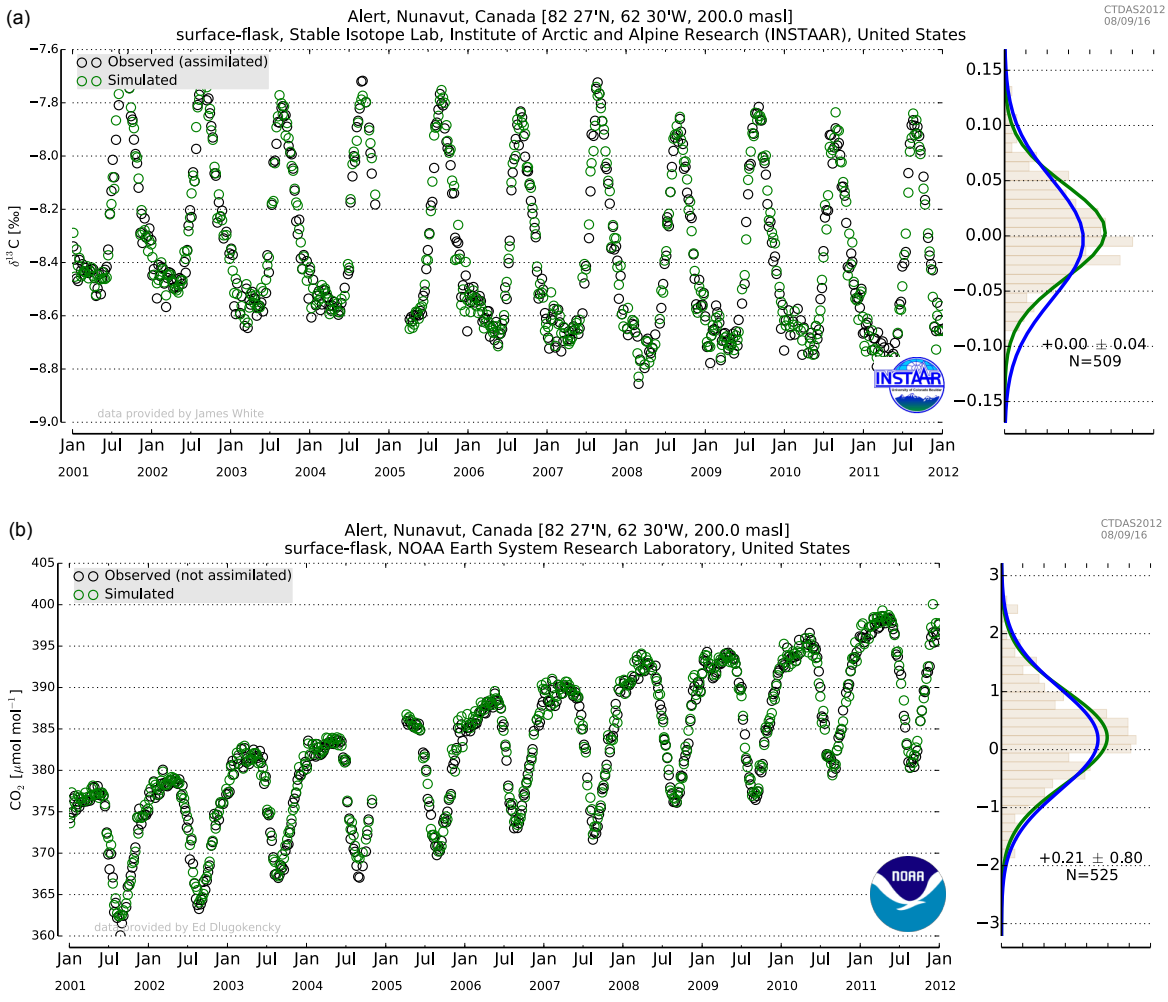

Figure 8. Comparison of two different inversion experiments at Alert (ALT, Canada). The top panel displays $\delta^{13}C$ observations (black circles) together with simulated $\delta^{13}C$ from NEW−CO2C13 (green circles). The top right panel displays the probability density functions (PDFs) of the residuals between NEW−CO2C13 and observed (green) and between TRAD−CO2 and observed (blue). The lower panel displays independent flask measurements (not used in the assimilation) of CO_2 (black circles) at Alert with simulated CO_2 from NEW−CO2C13 (green circles). Notice the almost identical distribution of the residual PDFs between NEW−CO2C13 and TRAD−CO2 inversion techniques.

where the drought index was negative over the mountain states, the impact on the carbon cycle was strongest over the eastern forests of the United States. In these forest ecosystems, CO_2 exchange is much stronger than over the mountains, and hence their impact on atmospheric $\delta^{13}C$ as well.

Notice that the prior net carbon sink is underestimated in comparison to the optimization because SiBCASA assumes a near steady state between GPP and TER (Fig. 10). SiBCASA was in fact able to simulate small carbon uptake anomalies during the reported droughts using its own environmental response parameterizations. However, it lacked a substantial amount of interannual variability in NEE and Δ_{ph} and lacked a strong correlation of Δ_{ph} with SPEI (Fig. 11). This suggests a potential absence of an important coupling between the hydrology and carbon discrimination processes in the model.

4 Discussion and conclusions

We developed a new application of the CarbonTracker data assimilation system that simulates two atmospheric tracers simultaneously: CO_2 and the $\delta^{13}C$ isotope signature of CO_2. We used measurements of both tracers to optimize the net ocean and land carbon exchange fluxes and the land discrimination parameter Δ_{ph}. The annual reductions in Δ_{ph} were up 0.75 ‰ and exceeded the 1σ SD of the IAV over 11 years in the North American domain (16.4 ± 0.3 ‰). We interpret these negative anomalies in Δ_{ph} as possible reductions of the intercellular CO_2 levels and relative increases in the intercellular $^{13}CO_2/^{12}CO_2$ ratio, resulting from stomatal closure due to drought stress on the leaf level. This is the most plausible explanation as most other factors that affect Δ_{ph} are (a) included a priori in the SiBCASA biosphere model, such as

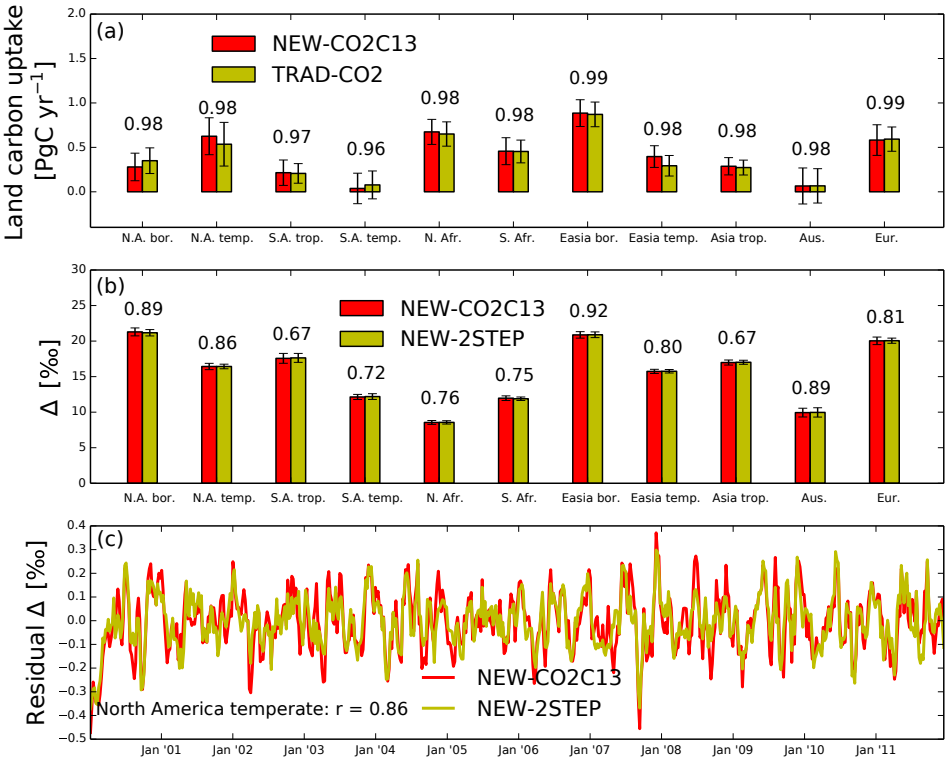

Figure 9. (a) the 11 year mean land carbon uptake ($\mathrm{Pg\,C\,yr^{-1}}$) for each TransCom region with estimates from the nonlinear NEW−CO2C13 inversion (red) and estimates from the linear TRAD−CO2 inversion (yellow). Error bars depict 1σ SD of the flux IAV. The 11 year correlation coefficients r between the two inversion methods are given on top of the bars. These correlations are based on the 3 month boxcar mean anomalies after subtracting the seasonal cycle. **(b)** Comparison of Δ_{ph} (‰) between the NEW−CO2C13 inversion and the linear NEW−2STEP inversion. We again provide IAV error bars and correlation coefficients between inversion methods. **(c)** The 3 month boxcar mean anomalies in Δ_{ph} for the North America temperate TransCom region to illustrate the high degree of similarity between both inversion methods ($r = 0.86$).

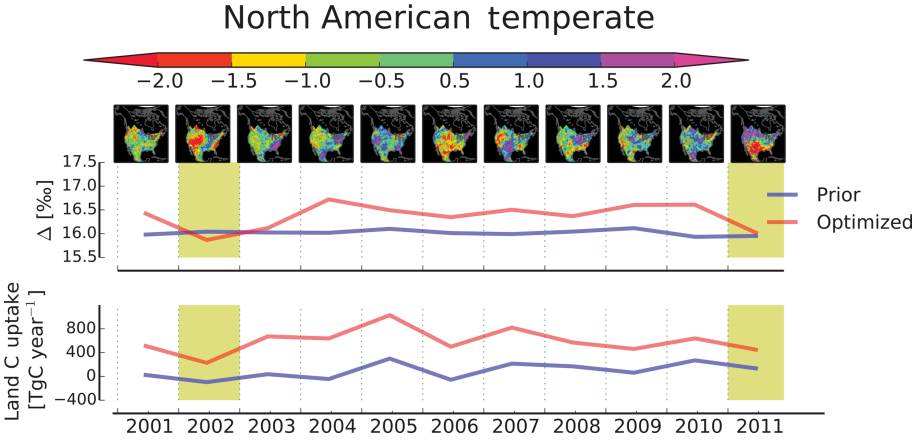

Figure 10. Top panels: the annual averaged Standardized Precipitation and Evaporation Index (SPEI) estimated for the North American temperate domain (map inserts). Middle panel: the annual GPP weighted averaged Δ_{ph} (‰) of vegetation against $^{13}CO_2$ from NEW−CO2C13 (red) and SiBCASA (blue) estimated for the same domain. It illustrates the summertime isoforcing of $\delta^{13}C$ towards the atmosphere (as wintertime Δ_{ph} has no impact on atmospheric $\delta^{13}C$). Lower panel: net carbon uptake ($\mathrm{TgC\,yr^{-1}}$) from NEW−CO2C13 (red) and SiBCASA (blue) estimated for the same domain. The yellow shaded years (2002 and 2011) indicate significant drought conditions as recorded in SPEI and other independent reports (e.g., Seager, 2010; Schwalm et al., 2012; Long et al., 2013). These droughts correlate with reductions in annual mean Δ_{ph}, and reductions in the estimated carbon sinks as reported in Peters et al. (2007).

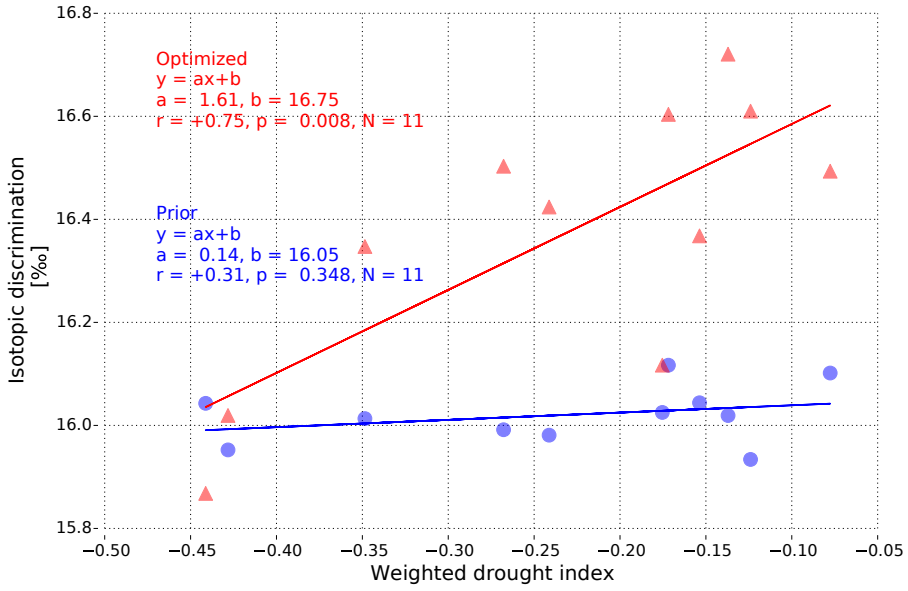

Figure 11. Weighted SPEI drought index (WDI) versus annual mean isotopic discrimination Δ_{ph} integrated over the North American temperate domain. Results from the SiBCASA biosphere model (blue circles) show no significant correlation between Δ_{ph} and large-scale droughts, while the simultaneous optimization of carbon sinks and Δ_{ph} with atmospheric CO_2 and $\delta^{13}C$ observations (red triangles) suggests a highly significant correlation can be derived. The slope of the red regression line is 1.61 ‰/WDI ($p = 0.008$, 95% confidence interval of a two-sided distribution with 9 degrees of freedom). The SiBCASA slope is, however, not significantly different from zero ($p \gg 0.05$). The integrated Δ_{ph} values are GPP-weighted per grid box as in Fig. 10. WDI is based on the SPEI index but area weighted to give years with large serried areas that experienced severe droughts (with SPEI smaller than −1.2) more leverage.

the effects of IAV on the strength of photosynthesis over C_3 and C_4 vegetation; (b) the variations in mesophyll conductance are not expected to vary much from year-to-year, such as ecosystem composition; or (c) the variations in mesophyll conductance would enhance the intercellular CO_2 levels (and thus Δ_{ph}) rather than reduce it, such as increased radiance of the leaves under reduced cloud cover. This suggests the possibility that the impact of environmental stress on stomatal conductance and carbon uptake is much larger than currently simulated by the widely used drought parameterizations in terrestrial biosphere models. These parameterizations are often derived from laboratory observations or plot-scale observations that often aggregate poorly over much larger scales. Our first results suggest that a data assimilation system that uses the global atmospheric $\delta^{13}C$ record, in concert with the CO_2 record, can offer new insights on large-scale drought dynamics of the coupled vegetation–atmosphere system.

It is unlikely that our terrestrial biosphere model will reproduce the new large-scale atmospheric constraints on NEE and Δ_{ph} with a simple adjustment of the currently used drought response parameterizations (such as stomatal conductance and soil water stress inhibition functions). We experimented with a different stomatal conductance model based on vapor pressure deficit (VPD; Leuning, 1995) rather than relative humidity as it was shown to better predict changes in the isotopic composition in tree rings (Ballantyne et al., 2010). This modification, however, did not change the annual covariation between NEE and Δ_{ph} in SiBCASA. In addition, modifications in the soil water stress function of SiBCASA, which impacts Δ_{ph} through mesophyll conductance (Seibt et al., 2008) also had little impact on annual variations in Δ_{ph}. Instead, SiBCASA shows minimal dynamic range in the hydrological drivers of drought stress. This was also concluded using satellite-observed soil moisture in SiBCASA over boreal EurAsia (van der Molen et al., 2016). That means our model is potentially (a) too homogenous regarding its plant and soil characteristics; (b) suffering from a too simple hydrological formulation for runoff and interception; (c) lacking realism in simulating the latency of ecosystem recovery after a severe drought; (d) misrepresenting effects of root-zone soil-moisture stress, as was also diagnosed for the Amazon by Harper et al. (2010) for the closely related SiB model; or (e) suffering from an even more fundamental problem inside the A–g_s model where c_i/c_a and c_c/c_a are calculated. In SiBCASA, the soil moisture limitations are applied by first downscaling assimilation rate (A), V_{max}, and mesophyll conductance, after which the balance is calculated between A, stomatal conductance (g_s), and c_c/c_a. In Egea et al. (2011) this approach was shown to conserve incorrectly intrinsic water-use efficiency (iWUE $= A/g_s$) and Δ_{ph} during droughts. However, initial tests show that a direct coupling of soil moisture stress to g_s would affect SiBCASA's iWUE (and Δ_{ph}) much stronger and more favorable during droughts (E. van Schaik, personal communication, 2017). The lack of

variability in simulated atmospheric $\delta^{13}C$ found in van der Velde et al. (2013) could well be (partially) ascribed to the lack of sensitivity towards soil moisture stress in SiBCASA. There is also evidence that the conventional use of land cover types in biosphere models does not adequately describe the spatial variations in carbon exchange (Bloom et al., 2016).

As with any data assimilation system, the number of available observations largely determines the assimilation system's ability to retrieve meaningful signals. Our current method relies on atmospheric $\delta^{13}C$ anomalies that affect multiple monitoring sites at the same time due to low signal-to-noise ratios at each site, but the network coverage over many parts of the world is still sparse. The increase in the number of measurement sites, and the addition of $\delta^{13}C$ to many existing ones, particularly in sparsely populated areas could benefit CTDAS-C13 greatly. New measurement efforts are currently underway to improve our observational coverage in these sparsely sampled areas. Regular measurements of CO_2 from aircraft vertical profiles have recently commenced at four different sites above the Amazon. These data have provided new insights on the carbon cycle under drought conditions (Gatti et al., 2014). These new measurements were successfully used in an application of CTDAS (van der Laan-Luijkx et al., 2015) and confirmed that the Amazonian CO_2 uptake by vegetation was indeed reduced during the severe 2010 drought. Furthermore, some coauthors are currently involved in a new collaborative effort to provide the first high-precision measurements of $\delta^{13}C$ and other isotopes in CO_2 from a large number of air samples collected over the Amazon basin. Using an assimilation system similar to that described here, these data would bolster our ability to quantify seasonal to interannual changes in the Amazonian carbon balance and better understand the influence of drought stress on NEE.

The retrieved correlation between NEE and Δ_{ph} in the Northern Hemisphere was derived from atmospheric $\delta^{13}C$ observations through our new dual-species approach, and thereby provided new insights on the land–atmosphere coupling of water and carbon on continental and hemispheric scales. The unconstrained SiBCASA model does not show a large enough response to drought both in terms of NEE and Δ_{ph}. The correlation between droughts and Δ_{ph} over the North American temperate domain (Fig. 10) can only be demonstrated after optimizing NEE and Δ_{ph} by applying atmospheric $\delta^{13}C$ and CO_2 constraints together. We emphasize that the reported correlations remain robust and significant even when changing the atmospheric transport characteristics (i.e., convection fields from ECMWF ERA-Interim meteorology vs. default TM5 convection scheme), the optimization method (nonlinear vs. linear 2-step), and when changing the assumed model–data errors of our data assimilation system.

A potential problem with the current framework is that we cannot account for changes in the terrestrial isodisequilibrium flux. In Eq. (1), we forced all missing isotopic variability into term $N_b\epsilon_{ph}$ without considering additional variability from the isodisequilibrium term. Photosynthetic discrimination is also responsible for a portion of the variability in the terrestrial isodisequilibrium flux (van der Velde et al., 2013), but the extent is hard to quantify. The δ_b^{eq} signature (i.e., the biosphere signature that is in equilibrium with the atmosphere) is a function of the current δ_a and Δ_{ph}, two quantities that ultimately exert influence on δ_b as the isotopic signal carries through the series of carbon reservoirs (i.e., leaves, stems, roots, and ultimately the soils). The absence of direct adjustments to the disequilibrium flux could mean we aliased erroneously isotopic signals only onto the net flux term of the budget. In light of recent observational evidence, the variability in the disequilibrium term might be of more importance than recently thought. Bowling et al. (2014) showed with δ_a measurements that the disequilibrium flux can become negative locally due to humidity-induced changes in Δ_{ph}. We found that these effects on the Δ_{ph} estimate are likely small mainly because gross flux variability is fundamentally limited and dampened by the large reservoir sizes from which it comes. In an experiment with SiBCASA where we allowed extra uncertainty in respiration and Δ_{ph} to drive through the disequilibrium isoflux we indeed found an increase in variability in the disequilibrium term, necessitating 10 % less Δ_{ph} variability to keep a closed $\delta^{13}C$ budget. This indicates that allowing for errors in the disequilibrium fluxes, the variations in the estimated Δ_{ph} parameter might be slightly smaller or larger than estimated with CTDAS-C13, but nonetheless still twice as large than estimated with SiBCASA. On one hand, using a more simplified but physically consistent set of equations only based on gross fluxes (GPP and TER) to express the rate of change of δ_a would eliminate the need for a disequilibrium term. On the other hand, this would complicate the closing of the CO_2 budget as it necessitates a way to effectively separate these two gross fluxes.

It is worth mentioning that the carbon residence time in land ecosystems is highly uncertain, and therefore the gross CO_2 exchange as well. Welp et al. (2011) suggested that the current popular estimate of global GPP of $120\,Pg\,C\,yr^{-1}$, which is also predicted by SiBCASA, may be a lower limit and could in reality be as large as $175\,Pg\,C\,yr^{-1}$ to reflect faster turnover of carbon in the vegetation and soils. Such uncertainties were also underlined by Carvalhais et al. (2014) who found that higher precipitation rates are associated with faster carbon turnover, but that global modeled turnover is in fact often underestimated. We make a cautious conjecture that if GPP is in fact as large as claimed by Welp et al. (2011), and heterotrophic respiration is large too, it will partly explain the current underestimation in the modeled disequilibrium fluxes, which are a function of TER and ocean CO_2 outgassing. In this study, we closed the gap with a predetermined scaling factor of 1.2 on the disequilibrium fluxes for oceans and land without assuming actual changes in GPP, TER, or Δ_{ph}. We could, therefore, benefit from a more integrated as-

similation system where we are using atmospheric data to simultaneously optimize for terrestrial model parameters that exert an influence on GPP, TER, and carbon turnover. The CTDAS modular design (van der Laan-Luijkx et al., 2017) makes it now more straightforward to develop and implement such additional improvements.

To conclude, this study showed there is significant potential to use atmospheric CO_2 and $\delta^{13}C$ data as constraints on plant NEE and isotopic discrimination using a dual-species assimilation platform. Signals that would otherwise be lost in a single tracer data assimilation system, such as the possibility of a drought-driven covariation between isotope discrimination and NEE or the separation of GPP from NEE, can potentially be detected in the described dual-species application of CTDAS. Continued and additional measurements of atmospheric $\delta^{13}C$ and CO_2, especially in future assimilation systems where biosphere model parameters are directly optimized, should help us better understand the hydrological and biogeochemical interactions between the atmosphere and vegetation.

Code availability. The CTDAS-C13 and TM5 source code are made available online (ftp://ftp.cmdl.noaa.gov/user/ivar/CTDAS_C13_sourcecode) (NOAA, 2018). More detailed model descriptions and information to run the code are available on the following websites: http://www.carbontracker.eu and http://tm.knmi.nl/index.php/Main_Page.

Author contributions. IvdV, WP, and JM designed the study. IvdV, KS, WP, and MvdM built the inverse and forward modeling frameworks. PT, BV, and JW were responsible for the $\delta^{13}C$ and CO_2 measurement program. IvdV performed the analysis and wrote the main text. All authors gave input on the final manuscript.

Competing interests. The authors declare that they have no conflict of interest.

Acknowledgements. This study was financially supported by the Netherlands Organization for Scientific Research (NWO-VIDI: 864.08.012), by the Visiting Fellows Program of the Cooperative Institute for Research in Environmental Sciences, and by the National Computing Facilities Foundation (NCF project SH-060) for the use of supercomputing facilities.

Edited by: Alexander Archibald
Reviewed by: Peter Rayner and one anonymous referee

References

Alden, C. B., Miller, J. B., and White, J. W. C.: Can bottom-up ocean CO_2 fluxes be reconciled with atmospheric ^{13}C observations?, Tellus B, 62, 369–388, https://doi.org/10.1111/j.1600-0889.2010.00481.x, 2010.

Andres, R. J., Marland, G., Boden, T. A., and Bischof, S.: Carbon dioxide emissions from fossil fuel consumption and cement manufacture, 1751–1991, and an estimate of their isotopic composition and latitudinal distribution, in: The Carbon Cycle, edited by: Wigley, T. and Schimel, D., Cambridge University Press, Cambridge, UK,53–62, 2000.

Ball, J. T.: An analysis of stomatal conductance, Ph. D. thesis, Stanford University, Stanford, CA, US, 1988.

Ballantyne, A. P., Miller, J. B., and Tans, P. P.: Apparent seasonal cycle in isotopic discrimination of carbon in the atmosphere and biosphere due to vapor pressure deficit, Global Biogeochem. Cy., 24, GB3018, https://doi.org/10.1029/2009GB003623, 2010.

Basu, S., Miller, J. B., and Lehman, S.: Separation of biospheric and fossil fuel fluxes of CO_2 by atmospheric inversion of CO_2 and $^{14}CO_2$ measurements: Observation System Simulations, Atmos. Chem. Phys., 16, 5665–5683, https://doi.org/10.5194/acp-16-5665-2016, 2016.

Bloom, A. A., Exbrayat, J.-F., van der Velde, I. R., Feng, L., and Williams, M.: The decadal state of the terrestrial carbon cycle: global retrievals of terrestrial carbon allocation, pools, and residence times, P. Natl. Acad. Sci. USA, 113, 1285–1290, 2016.

Booth, B. B., Jones, C. D., Collins, M., Totterdell, I. J., Cox, P. M., Sitch, S., Huntingford, C., Betts, R. A., Harris, G. R., and Lloyd, J.: High sensitivity of future global warming to land carbon cycle processes, Environ. Res. Lett., 7, 024002, https://doi.org/10.1088/1748-9326/7/2/024002, 2012.

Bowling, D. R., Ballantyne, A. P., Miller, J. B., Burns, S. P., Conway, T. J., Menzer, O., Stephens, B. B., and Vaughn, B. H.: Ecological processes dominate the ^{13}C land disequilibrium in a Rocky Mountain subalpine forest, Global Biogeochem. Cy., 28, 352–370, https://doi.org/10.1002/2013GB004686, 2014.

Bozhinova, D., van der Molen, M. K., van der Velde, I. R., Krol, M. C., van der Laan, S., Meijer, H. A. J., and Peters, W.: Simulating the integrated summertime $\Delta^{14}CO_2$ signature from anthropogenic emissions over Western Europe, Atmos. Chem. Phys., 14, 7273–7290, https://doi.org/10.5194/acp-14-7273-2014, 2014.

Bruhwiler, L., Dlugokencky, E., Masarie, K., Ishizawa, M., Andrews, A., Miller, J., Sweeney, C., Tans, P., and Worthy, D.: CarbonTracker-CH_4: an assimilation system for estimating emissions of atmospheric methane, Atmos. Chem. Phys., 14, 8269–8293, https://doi.org/10.5194/acp-14-8269-2014, 2014.

Carvalhais, N., Forkel, M., Khomik, M., Bellarby, J., Jung, M., Migliavacca, M., Mu, M., Saatchi, S., Santoro, M., Thurner, M., Weber, U., Ahrens, B., Beer, C., Cescatti, A., Randerson, J. T., and Reichstein, M.: Global covariation of carbon turnover times with climate in terrestrial ecosystems, Nature, 514, 213–217, 2014.

Ciais, P., Tans, P. P., White, J., and Trolier, M.: Partitioning of ocean and land uptake of CO_2 as inferred by $\delta^{13}C$ measurements from the NOAA Climate Monitoring and Diagnostics Laboratory Global Air Sampling Network, J. Geophys. Res., 100, 5051–5070, 1995.

Ciais, P., Reichstein, M., Viovy, N., Granier, A., Ogée, J., Allard, V., Aubinet, M., Buchmann, N., Bernhofer, C., Carrara, A., Chevallier, F., De Noblet, N., Friend, A. D., Friedlingstein, P., Grünwald, T., Heinesch, B., Keronen, P., Knohl, A., Krinner, G., Loustau, D., Manca, G., Matteucci, G., Miglietta, F., Ourcival, J. M., Papale, D., Pilegaard, K., Rambal, S., Seufert, G., Soussana, J. F., Sanz, M. J., Schulze, E. D., Vesala, T., and Valentini, R.: Europe-wide reduction in primary productivity caused by the heat and drought in 2003, Nature, 437, 529–533, 2005.

Collatz, G. J., Ball, J., Grivet, C., and Berry, J. A.: Physiological and environmental regulation of stomatal conductance, photosynthesis and transpiration: a model that includes a laminar boundary layer, Agr. Forest Meteorol., 54, 107–136, 1991.

Collatz, G. J., Ribas-Carbo, M., and Berry, J. A.: Coupled photosynthesis-stomatal conductance model for leaves of C_4 plants, Aust. J. Plant Physiol., 19, 519–538, 1992.

Commane, R., Meredith, L. K., Baker, I. T., Berry, J. A., Munger, J. W., Montzka, S. A., Templer, P. H., Juice, S. M., Zahniser, M. S., and Wofsy, S. C.: Seasonal fluxes of carbonyl sulfide in a mid-latitude forest, P. Natl. Acad. Sci. USA, 112, 14162–14167, 2015.

Dai, A.: Increasing drought under global warming in observations and models, Nat. Clim. Change, 3, 52–58, https://doi.org/10.1038/nclimate1633, 2012.

Dee, D. P., Uppala, S., Simmons, A., Berrisford, P., Poli, P., Kobayashi, S., Andrae, U., Balmaseda, M. A., Balsamo, G., Bauer, P., Bechtold, P., Beljaars, A. C. M., van de Berg, L., Bidlot, J.-R., Bormann, N., Delsol, C., Dragani, R., Fuentes, M., Geer, A., Haimberger, L., Healy, S., Hersbach, H., Hólm, E. V., Isaksen, L., Kållberg, P. W., Köhler, M., Matricardi, M., McNally, A., Monge-Sanz, B. M., Morcrette, J.-J., Peubey, C., De Rosnay, P., Tavolato, C., Thépaut, J.-J., and Vitart, F.: The ERA-interim reanalysis: configuration and performance of the data assimilation system, Q. J. Roy. Meteor. Soc., 137, 553–597, https://doi.org/10.1002/qj.828, 2011.

Egea, G., Verhoef, A., and Vidale, P. L.: Towards an improved and more flexible representation of water stress in coupled photosynthesis–stomatal conductance models, Agr. Forest Meteorol., 151, 1370–1384, https://doi.org/10.1016/j.agrformet.2011.05.019, 2011.

Ekblad, A. and Högberg, P.: Natural abundance of ^{13}C in CO_2 respired from forest soils reveals speed of link between tree photosynthesis and root respiration, Oecologia, 127, 305–308, https://doi.org/10.1007/s004420100667, 2001.

Farquhar, G. D., Caemmerer, S. V., and Berry, J. A.: A biochemical-model of photosynthetic CO_2 assimilation in leaves of C_3 species, Planta, 149, 78–90, 1980.

Farquhar, G. D., O'Leary, M. H., and Berry, J. A.: On the relationship between carbon isotope discrimination and the intercellular carbon dioxide concentration in leaves, Aust. J. Plant Physiol., 9, 121–137, 1982.

Farquhar, G. D., Ehleringer, J. R., and Hubrick, K. T.: Carbon isotope discrimination and photosynthesis, Annu. Rev. Plant Phys., 40, 503–537, 1989.

Flexas, J., Ribas-Carbo, M., Diaz-Espej, A., Galmes, J., and Medrano, H.: Mesophyll conductance to CO_2: current knowledge and future prospects, Plant Cell Environ., 31, 602–621, 2008.

Friedlingstein, P., Cox, P., Betts, R., Bopp, L., von Bloh, W., Brovkin, V., Cadule, P., Doney, S., Eby, M., Fung, I., Bala, G., John, J., Jones, C., Joos, F., Kato, T., Kawamiya, M., Knorr, W., Lindsay, K., Matthews, H. D., Raddatz, T., Rayner, P., Reick, C., Roeckner, E., Schnitzler, K.-G., Schnur, R., Strassmann, K., Weaver, A. J., Yoshikawa, C., and Zeng, N.: Climate–carbon cycle feedback analysis: results from the C4MIP model intercomparison, J. Climate, 19, 3337–3353, 2006.

Fung, I., Field, C. B., Berry, J. A., Thompson, M. V., Randerson, J. T., Malmström, C. M., Vitousek, P. M., James Collatz, G., Sellers, P. J., Randall, D. A., Denning, A. S., Badeck, F., and John, J.: Carbon 13 exchanges between the atmosphere and biosphere, Global Biogeochem. Cy., 11, 507–533, 1997.

Gatti, L. V., Gloor, M., Miller, J. B., Doughty, C. E., Malhi, Y., Domingues, L. G., Basso, L. S., Martinewski, A., Correia, C. S., Borges, V. F., Freitas, S., Braz, R., Anderson, L. O., Rocha, H., Grace, J., Phillips, O. L., and Lloyd, J.: Drought sensitivity of Amazonian carbon balance revealed by atmospheric measurements, Nature, 506, 76–80, https://doi.org/10.1038/nature12957, 2014.

Gruber, N., Keeling, C. D., Bacastow, R. B., Guenther, P. R., Lueker, T. J., Wahlen, M., Meijer, H. A. J., Mook, W. G., and Stocker, T. F.: Spatiotemporal patterns of carbon-13 in the global surface oceans and the oceanic Suess effect, Global Biogeochem. Cy., 13, 307–335, 1997.

Gurney, K. R., Law, R. M., Denning, A. S., Rayner, P. J., Baker, D., Bousquet, P., Bruhwiler, L., Chen, Y.-H., Ciais, P., Fan, S., Fung, I. Y., Gloor, M., Heimann, M., Higuchi, K., John, J., Maki, T., Maksyutov, S., Masarie, K., Peylin, P., Prather, M., Pak, B. C., Randerson, J., Sarmiento, J., Taguchi, S, Takahashi, T., and Yuen, C.-W.: Towards robust regional estimates of CO_2 sources and sinks using atmospheric transport models, Nature, 415, 626–630, 2002.

Harper, A. B., Denning, A. S., Baker, I. T., Branson, M. D., Prihodko, L., and Randall, D. A.: Role of deep soil moisture in modulating climate in the Amazon rainforest, Geophys. Res. Lett., 37, L05802, https://doi.org/10.1029/2009GL042302, 2010.

Hoffman, F. M., Randerson, J. T., Arora, V. K., Bao, Q., Cadule, P., Ji, D., Jones, C. D., Kawamiya, M., Khatiwala, S., Lindsay, K., Obata, A., Shevliakova, E., Six, K. D., Tjiputra, J. F., Volodin, E. M., and Wu, T.: Causes and implications of persistent atmospheric carbon dioxide biases in Earth System Models, J. Geophys. Res.-Biogeo., 119, 141–162, 2014.

Jacobson, A. R., Gruber, N., Sarmiento, J. L., Gloor, M., and Mikaloff Fletcher, S. E.: A joint atmosphere–ocean inversion for surface fluxes of carbon dioxide: I. Methods and global-scale fluxes, Global Biogeochem. Cy., 21, GB1019, https://doi.org/10.1029/2005GB002556, 2007.

Keeling, C. D. and Revelle, R.: Effects of El Nino/Southern Oscillation on the atmospheric content of carbon dioxide, Meteoritics, 20, 437–450, 1985.

Keeling, C. D., Bacastow, R. B., Carter, A. F., Piper, S. C., Whorf, T. P., Heimann, M., Mook, W. G., and Roeloffzen, H.: A three-dimensional model of atmospheric CO_2 transport based on observed winds: 1. Analysis of observational data, in: Aspects of Climate Variability in the Pacific and the Western Americas, edited by: Peterson, D. H., American Geophysical Union, Washington, D.C., United States, 165–236, 1989.

Kretschmer, R., Gerbig, C., Karstens, U., and Koch, F.-T.: Error characterization of CO_2 vertical mixing in the atmospheric transport model WRF-VPRM, Atmos. Chem. Phys., 12, 2441–2458, https://doi.org/10.5194/acp-12-2441-2012, 2012.

Krol, M., Houweling, S., Bregman, B., van den Broek, M., Segers, A., van Velthoven, P., Peters, W., Dentener, F., and Bergamaschi, P.: The two-way nested global chemistry-transport zoom model TM5: algorithm and applications, Atmos. Chem. Phys., 5, 417–432, https://doi.org/10.5194/acp-5-417-2005, 2005.

Leuning, R.: A critical appraisal of a combined stomatal photosynthesis model for C_3 plants, Plant Cell Environ., 18, 339–355, https://doi.org/10.1111/j.1365-3040.1995.tb00370.x, 1995.

Long, D., Scanlon, B. R., Longuevergne, L., Sun, A.-Y., Fernando, D. N., and Save, H.: GRACE satellites monitor large depletion in water storage in response to the 2011 drought in Texas, Geophys. Res. Lett., 40, 3395–3401, https://doi.org/10.1002/grl.50655, 2013.

Masarie, K. A., Peters, W., Jacobson, A. R., and Tans, P. P.: ObsPack: a framework for the preparation, delivery, and attribution of atmospheric greenhouse gas measurements, Earth Syst. Sci. Data, 6, 375–384, https://doi.org/10.5194/essd-6-375-2014, 2014.

Miller, S. M., Hayek, M. N., Andrews, A. E., Fung, I., and Liu, J.: Biases in atmospheric CO_2 estimates from correlated meteorology modeling errors, Atmos. Chem. Phys., 15, 2903–2914, https://doi.org/10.5194/acp-15-2903-2015, 2015.

NOAA: CTDAS-C13 and TM5 source code, available at: ftp://ftp.cmdl.noaa.gov/user/ivar/CTDAS_C13_sourcecode, last access: 15 January 2018.

O'Leary, M. H.: Carbon isotopes in photosynthesis, fractionation techniques may reveal new aspects of carbon dynamics in plants, BioScience, 38, 328–336, 1988.

Olson, J. S., Watts, J. A., and Allsion, L. J.: Major World Ecosystem Complexes Ranked by Carbon in Live Vegetation: a Database, ORNL/CDIAC-134, NDP-017, Carbon Dioxide Information Analysis Center, U.S. Department of Energy, Oak Ridge National Laboratory, Oak Ridge, Tennessee, USA, revised 2001, 1985.

Ometto, J. P. H. B., Flanagan, L. B., Martinelli, L. A., Moreira, M. Z., Higuchi, N., and Ehleringer, J. R.: Carbon isotope discrimination in forest and pasture ecosystems of the Amazon Basin, Brazil, Global Biogeochem. Cy., 16, 1109, https://doi.org/10.1029/2001GB001462, 2002.

Peters, W., Miller, J. B., Whitaker, J., Denning, A. S., Hirsch, A., Krol, M. C., Zupanski, D., Bruhwiler, L., and Tans, P. P.: An ensemble data assimilation system to estimate CO_2 surface fluxes from atmospheric trace gas observations, J. Geophys. Res., 110, D24304, https://doi.org/10.1029/2005JD006157, 2005.

Peters, W., et. al.: An atmospheric perspective on North American carbon dioxide exchange: CarbonTracker, P. Natl. Acad. Sci. USA, 107, 18,925–18,930, 2007.

Peters, W., Krol, M. C., van der Werf, G. R., Houweling, S., Jones, C. D., Hughes, J., Schaefer, K., Masarie, K. A., Jacobson, A. R., Miller, J. B., Cho, C. H., Ramonet, M., Schmidt, M., Ciattaglia, L., Apadula, F., Heltai, D., Meinhardt, F., di Sarra, A. G., Piacentino, S., Sferlazzo, D., Aalto, T., Hatakka, J., Ström, J., Haszpra, L., Meijer, H. A. J., van der Laan, S., Neubert, R. E. M., Jordan, A., Rodó, X., Morguí, J.-A., Vermeulen, A. T., Popa, E., Rozanski, K., Zimnoch, M., Manning, A. C., Leuenberger, M., Uglietti, C., Dolman, A. J., Ciais, P., Heimann, M., and Tans, P. P.: Seven years of recent European net terrestrial carbon dioxide exchange constrained by atmospheric observations, Glob. Change Biol., 16, 1317–1337, 2010.

Raczka, B., Duarte, H. F., Koven, C. D., Ricciuto, D., Thornton, P. E., Lin, J. C., and Bowling, D. R.: An observational constraint on stomatal function in forests: evaluating coupled carbon and water vapor exchange with carbon isotopes in the Community Land Model (CLM4.5), Biogeosciences, 13, 5183–5204, https://doi.org/10.5194/bg-13-5183-2016, 2016.

Rayner, P. J., Law, R. M., Allison, C. E., Francey, R. J., Trudinger, C. M., and Pickett-Heaps, C.: Interannual variability of the global carbon cycle (1992–2005) inferred by inversion of atmospheric CO_2 and $\delta^{13}CO_2$ measurements, Global Biogeochem. Cy., 22, GB3008, https://doi.org/10.1029/2007GB003068, 2008.

Rowlands, D. J., Frame, D. J., Ackerley, D., Aina, T., Booth, B. B., Christensen, C., Collins, M., Faull, N., Forest, C. E., Grandey, B. S.; Gryspeerdt, E., Highwood, E. J.; Ingram, W. J.; Knight, S., Lopez, A., Massey, N., McNamara, F., Meinshausen, N., Piani, C., Rosier, S. M., Sanderson, B. M., Smith, L. A., Stone, D. A., Thurston, M., Yamazaki, K., Hiro Yamazaki, Y., and Allen, M. R.: Broad range of 2050 warming from an observationally constrained large climate model ensemble, Nat. Geosci., 5, 256–260, 2012.

Schaefer, K., Collatz, G. J., Tans, P. P., Denning, A. S., Baker, I., Berry, J. A., Prihodko, L., Suits, N., and Philpott, A.: Combined Simple Biosphere/Carnegie–Ames–Stanford Approach terrestrial carbon cycle model, J. Geophys. Res., 113, G03034, https://doi.org/10.1029/2007JG000603, 2008.

Scholze, M., Kaplan, J. O., Knorr, W., and Heimann, M.: Climate and interannual variability of the atmosphere–biosphere $^{13}CO_2$ flux, Geophys. Res. Lett., 30, 1097, https://doi.org/10.1029/2002GL015631, 2003.

Schwalm, C. R., Williams, C. A., Schaefer, K., Baldocchi, D., Black, T. A., Goldstein, A. H., Law, B. E., Oechel, W. C., Tha Paw U, K., and Scott, R. L.: Reduction in carbon uptake during turn of the century drought in western North America, Nature Geosci., 5, 551–556, 2012.

Seager, R.: The turn of the Century North American Drought: global context, dynamics, and past analogs, J. Climate, 20, 5527–5552, 2010.

Seibt, U., Rajabi, A., Griffiths, H., and Berry, J. A.: Carbon isotopes and water use efficiency: sense and sensitivity, Oecologia, 155, 441–454, 2008.

Sellers, P. J., Randall, D. A., Collatz, G. J., Berry, J. A., Field, C. B., Dazlich, D. A., Zhang, C., Collelo, G. D., and Bounoua, L.: A revised land surface parameterization (SiB2) for atmospheric GCMs. Part I: Model formulation, J. Climate, 9, 676–705, 1996.

Still, C. J., Berry, J. A., Collatz, G. J., and DeFries, R. S.: Global distribution of C_3 and C_4 vegetation: carbon cycle implications, Global Biogeochem. Cy., 17, 1006, https://doi.org/10.1029/2001GB001807, 2003.

Suits, N., Denning, A., Berry, J., and Still, C.: Simulation of carbon isotope discrimination of the terrestrial biosphere, Global Biogeochem. Cy., 19, GB1017, https://doi.org/10.1029/2003GB002141, 2005.

Takahashi, T., Sutherland, S. C., Wanninkhof, R., Sweeney, C., Feely, R. A., Chipman, D. W., Hales, B., Friederich, G., Chavez,

F., Sabine, C., Watson, A., Bakker, D. C. E., Schuster, U., Metzl ,N., Yoshikawa-Inoue, H., Ishii, M., Midorikawa, T., Nojiri, Y., Körtzinger, A., Steinhoff, T., Hoppema, M., Olafsson, J., Arnarson, T. S., Tilbrook, B., Johannessen, T., Olsen, A., Bellerby, R., Wong, C. S., Delille, B., Bates, N. R., de Baar, H. J. W.: Climatological mean and decadal change in surface ocean pCO_2, and net sea–air CO_2 flux over the global oceans, Deep-Sea Res. Pt. II, 56, 554–577, 2009.

Tans, P. P., Berry, J. A., and Keeling, R. F.: Oceanic $^{13}C/^{12}C$ observations – a new window on ocean CO_2 uptake, Global Biogeochem. Cy., 7, 353–368, 1993.

Tarantola, A.: Inverse Problem Theory and Methods for Model Parameter Estimation, Soc. for Ind., and Appl. Math., Philadelphia, Pa, 2005.

Tsuruta, A., Aalto, T., Backman, L., Hakkarainen, J., van der Laan-Luijkx, I. T., Krol, M. C., Spahni, R., Houweling, S., Laine, M., Dlugokencky, E., Gomez-Pelaez, A. J., van der Schoot, M., Langenfelds, R., Ellul, R., Arduini, J., Apadula, F., Gerbig, C., Feist, D. G., Kivi, R., Yoshida, Y., and Peters, W.: Global methane emission estimates for 2000–2012 from CarbonTracker Europe-CH4 v1.0, Geosci. Model Dev., 10, 1261–1289, https://doi.org/10.5194/gmd-10-1261-2017, 2017.

van der Laan-Luijkx, I. T., van der Velde, I. R., Krol, M. C., Gatti, L. V., Domingues, L. G., Correia, C. S. C., Miller, J. B., Gloor, M., van Leeuwen, T. T., Kaiser, J. W., Wiedinmyer, C., Basu, S., Clerbaux, C., and Peters, W.: Response of the Amazon carbon balance to the 2010 drought derived with CarbonTracker South America, Global Biogeochem. Cy., 29, 1092–1108, 2015.

van der Laan-Luijkx, I. T., van der Velde, I. R., van der Veen, E., Tsuruta, A., Stanislawska, K., Babenhauserheide, A., Zhang, H. F., Liu, Y., He, W., Chen, H., Masarie, K. A., Krol, M. C., and Peters, W.: The CarbonTracker Data Assimilation Shell (CTDAS) v1.0: implementation and global carbon balance 2001–2015, Geosci. Model Dev., 10, 2785–2800, https://doi.org/10.5194/gmd-10-2785-2017, 2017.

van der Molen, M. K., de Jeu, R. A. M., Wagner, W., van der Velde, I. R., Kolari, P., Kurbatova, J., Varlagin, A., Maximov, T. C., Kononov, A. V., Ohta, T., Kotani, A., Krol, M. C., and Peters, W.: The effect of assimilating satellite-derived soil moisture data in SiBCASA on simulated carbon fluxes in Boreal Eurasia, Hydrol. Earth Syst. Sci., 20, 605–624, https://doi.org/10.5194/hess-20-605-2016, 2016.

van der Sleen, P., Groenendijk, P., Vlam, M., Anten, N. P. R., Boom, A., Bongers, F., Pons, T. L., Terburg, G., and Zuidema, P. A.: No growth stimulation of tropical trees by 150 years of CO_2 fertilization but water-use efficiency increased, Nat. Geosci., 8, 24–28, https://doi.org/10.1038/ngeo2313, 2015.

van der Velde, I. R.: Studying biosphere–atmosphere exchange of CO_2 through Carbon-13 stable isotopes, PhD dissertation, Wageningen University, Wageningen, the Netherlands, 2015.

van der Velde, I. R., Miller, J. B., Schaefer, K., Masarie, K. A., Denning, S., White, J. W. C., Tans, P. P., Krol, M. C., and Peters, W.: Biosphere model simulations of interannual variability in terrestrial $^{13}C/^{12}C$ exchange, Global Biogeochem. Cy., 27, 637–649, 2013.

van der Velde, I. R., Miller, J. B., Schaefer, K., van der Werf, G. R., Krol, M. C., and Peters, W.: Terrestrial cycling of $^{13}CO_2$ by photosynthesis, respiration, and biomass burning in SiBCASA, Biogeosciences, 11, 6553–6571, https://doi.org/10.5194/bg-11-6553-2014, 2014.

Vicente-Serrano, S. M., Begueria, S., and Lopez-Moreno, J. I.: A multi-scalar drought index sensitive to global warming: The Standardized Precipitation Evapotranspiration Index – SPEI, J. Climate, 23, 1696–1718, 2010.

Wanninkhof, R.: Relationship between wind speed and gas exchange over the ocean, J. Geophys. Res, 97, 7373–7382, 1992.

Wehr, R., Munger, J. W., McManus, J. B., Nelson, D. D., Zahniser, M. S., Davidson, E. A., Wofsy, S. C., and Saleska, S. R.: Seasonality of temperate forest photosynthesis and daytime respiration, Nature, 534, 680–683, https://doi.org/10.1038/nature17966, 2016.

Welp, L. R., Keeling, R. F., Meijer, H. A., Bollenbacher, A. F., Piper, S. C., Yoshimura, K., Francey, R. J., Allison, C. E., and Wahlen, M.: Interannual variability in the oxygen isotopes of atmospheric CO_2 driven by El Nino, Nature, 477, 579–582, 2011.

Yang, X., Tang, J., Mustard, J. F., Lee, J.-E., Rossini, M., Joiner, J., Munger, J. W., Kornfeld, A., and Richardson, A. D.: Solar induced chlorophyll fluorescence that correlates with canopy photosynthesis on diurnal and seasonal scales in a temperate deciduous forest, Geophys. Res. Lett., 42, 2977–2987, https://doi.org/10.1002/2015GL063201, 2015.

Zhang, H. F., Chen, B. Z., van der Laan-Luijk, I. T., Machida, T., Matsueda, H., Sawa, Y., Fukuyama, Y., Langenfelds, R., van der Schoot, M., Xu, G., Yan, J. W., Cheng, M. L., Zhou, L. X., Tans, P. P., and Peters, W.: Estimating Asian terrestrial carbon fluxes from CONTRAIL aircraft and surface CO_2 observations for the period 2006–2010, Atmos. Chem. Phys., 14, 5807–5824, https://doi.org/10.5194/acp-14-5807-2014, 2014.

Zhang, J., Quay, P. D., and Wilbur, D. O.: Carbon isotope fractionation during gas-water exchange and dissolution of CO_2, Geochim. Cosmochim., 59, 107–114, 1995.